Review of Palaeobotany and Palynology 305 (2022) 104743

Contents lists available at ScienceDirect

Review of Palaeobotany and Palynology

journal homepage: www.elsevier.com/locate/revpalbo

Early Miocene redwood fossils from Inner Mongolia: CO_2 reconstructions and paleoclimate effects of a low Mongolian plateau

Jia-qi Liang [a,b], Qin Leng [b,*], Liang Xiao [a,*], Daianne F. Höfig [c], Dana L. Royer [d], Yi Ge Zhang [c], Hong Yang [b,*]

[a] School of Earth Science and Resources, Chang'an University, Xi'an 710054, China
[b] Laboratory for Terrestrial Environments, Bryant University, 1150 Douglas Pike, Smithfield, RI 02917, USA
[c] Department of Oceanography, Texas A&M University, College Station, TX 77843, USA
[d] Department of Earth and Environmental Sciences, Wesleyan University, Middletown, CT 06459, USA

ARTICLE INFO

Article history:
Received 13 March 2022
Received in revised form 25 July 2022
Accepted 31 July 2022
Available online 4 August 2022

Keywords:
Redwood
Ancient CO_2
Franks model
Early Miocene
Mongolian plateau
Asian monsoon

ABSTRACT

The early Miocene (~16–23 Ma) marks a critical transition in the Earth climate history from an Oligocene (~23–34 Ma) cooling trend towards the well-documented warm middle Miocene Climate Optimum at ~15 Ma. In eastern Asia, this transition links changes of key topographic features, such as the Tibetan plateau and the Mongolian plateau, and their impact on the reorganization of climate systems, such as the Eastern Asian summer monsoon. Yet the dynamics of the interplay among these factors remain poorly understood, precluding our understanding of future climate changes. Global temperatures during the early Miocene were warmer than the present day by 3–4 °C, which are seemingly incompatible with both the low (<300 ppm) and high (>800 ppm) ends of presently available reconstructions of atmospheric carbon dioxide (CO_2). Here we report a rare co-occurrence of two redwoods, *Metasequoia* and *Sequoia*, from sediments of the early Miocene Hannuoba Formation in Zhuozi County in China's Inner Mongolia at the southeastern margin of the current Mongolian plateau. The Zhuozi *Metasequoia* fossils possess uneven type cuticles, which dominate its living population but have rarely been reported throughout the abundant fossil record of this genus. By applying well-constrained Franks model parameters obtained from these redwood fossils using a cleared leaf epidermis method, we estimated the early Miocene CO_2 level at ~400 ppm, putting it at the lower end of the model requirement for sustaining a relatively warm global temperature during this period. Our Franks model estimates are ~100 ppm higher than that obtained using stomatal index method based on *Metasequoia* material, further confirming a systematic underestimation of ancient CO_2 using the *Metasequoia* stomatal index method reported in previous analyses. We recommend a re-examination of previous CO_2 reconstructions solely based upon *Metasequoia*'s inverse relationship between stomatal index and CO_2 concentrations. Ultimately, the occurrence of these redwood fossils in Inner Mongolia is consistent with a weak or muted Eastern Asian summer monsoon in the region with the absence of an elevated Mongolian plateau during the early Miocene. A shift of moisture sources for the region accompanying the change from a Westerlies-dominated climate to the present-day monsoon-dominated climate system occurred after the early Miocene time.

1. Introduction

Miocene (~5–23 Ma) was the time when the global climate cooled down from the Eocene (~33–56 Ma) warm-house state of high temperature and high carbon dioxide (CO_2) conditions but was still warmer than the present-day analog of Pliocene (2.4–5.4 Ma; Burke et al., 2018; Steinthorsdottir et al., 2021a). Early Miocene (~16–23 Ma) witnessed a general trend of increasing atmospheric CO_2 and global temperature, heralding the middle Miocene Climate Optimum (MCO) at ~15 Ma. Based upon the current rate of greenhouse gas emissions, if societies cannot limit Earth's anthropogenic temperature anomaly to 1.5–2 °C, the Earth systems may reach to the critical climate scenarios similar to the MCO, such as the high Representative Concentration Pathway (RCP) specified in the most recent IPCC report AR6 (Schellnhuber et al., 2016; Burke et al., 2018; IPCC, 2021). Therefore, a better understanding of the early Miocene paleoclimate, particularly its CO_2 concentrations and biotic responses, will allow us to better predict the future global climate change. Previous reconstructions of early Miocene CO_2 using various proxies generated highly-variable results, from median values below pre-industrial levels (270 ppm; Foster

* Corresponding authors.
E-mail addresses: qleng@bryant.edu (Q. Leng), youmu4@sina.com (L. Xiao), hyang@bryant.edu (H. Yang).

https://doi.org/10.1016/j.revpalbo.2022.104743

et al., 2012; Ji et al., 2018; Greenop et al., 2019) to high concentrations (500–1000 ppm; Lowenstein and Demicco, 2006; Tesfamichael et al., 2017; Londoño et al., 2018; Reichgelt et al., 2020) (See Supplementary Material Table S1). In contrast to the well-studied middle Miocene period, there is a significant gap in the CO_2 records for the early Miocene. Yet, CO_2 changes in this period have been linked to key global events such as the extensive erosion and weathering due to the uplift of the Tibetan plateau (Raymo and Ruddiman, 1992) and the critical transient Antarctic ice sheet (Levy et al., 2016; Greenop et al., 2019). Thus, more accurate CO_2 data from this period is urgently needed to fill the gaps and increase the resolution of the paleoclimatic conditions during these important global events.

In eastern Asia, the early Miocene is a critical timeframe for the reorganization of the main Asian climate systems, including Asian monsoons, desertification, and enhanced chemical weathering and exhumation, due to both orbital variability and tectonic topographic changes (Guo et al., 2002, 2008; Liu and Yin, 2002; Clift et al., 2008; Gébelin et al., 2013; Thomson et al., 2021; Yang et al., 2021). The onset of the Eastern Asian summer monsoon (EASM), in particular its strength and areas of influence during early Miocene, have been a subject of intense discussion and debate (An et al., 2001, 2005, 2015; Ding and Chan, 2005; Sun and Wang, 2005; Guo et al., 2002, 2008; Liu et al., 2011; Licht et al., 2014; Spicer et al., 2016; Tada et al., 2016; Zhang et al., 2017; Yu et al., 2018; Farnsworth et al., 2019). It has been proposed that the history of uplifts of several key topographic features (i.e., the northern Tibetan and Mongolian plateaus and the Tianshan Mountains) played essential roles in affecting regional climate change during the last 67 million years (Sun and Wang, 2005; Clift et al., 2008; Guo et al., 2008; Liu et al., 2011; Yu et al., 2018; Clift and Webb, 2018). Although the Mongolian plateau is smaller in size and lower in altitudes than the extensively-researched Tibetan plateau, it is a prominent topographic feature that influences modern-day climate in eastern Mongolia and northeastern China but has received relatively less attention until recently (Jolivet et al., 2007; Shi et al., 2015; Sha et al., 2015; White et al., 2018). While the timing of uplift for the Mongolian plateau and its climate effects remain unclear, modeling work suggests that the rise of the Mongolian plateau enhanced the strength of modern EASM in northern China (Tang et al., 2013; Zhang et al., 2017; White et al., 2018). The modern climate of the Zhuozi fossil site (from where our fossils were collected) at the eastern margin of the Mongolian plateau is under the strong influence of the interplay between the EASM and the westerly jet with most of the annual precipitation occurring during the summer times (Piao et al., 2018; Chen et al., 2020). As the two redwood genera, *Metasequoia* and *Sequoia,* of the current study are both sensitive to monsoonal climate (Zhang et al., 2015; Wang et al., 2019; Fan et al., 2020), the presence of their fossils at the current northernmost limit of EASM influence provides insights into the effect of the uplift of the Mongolian plateau to the region's climate system.

Metasequoia and *Sequoia* leafy branches are common components of the early Miocene fossil beds discovered from Erlongshan in Zhuozi County of China's Inner Mongolia. Because of their well-understood ecology, physiology, and paleobiology (Chaney, 1950; LePage et al., 2005; Yang and Hickey, 2007; Ma et al., 2005; Zhang et al., 2015; Wang et al., 2019; Fan et al., 2020), these two redwood fossils provide ideal material for a better understanding of paleoclimate and paleoenvironment during this critical Neogene time.

In this study, we use these fossils to reconstruct early Miocene CO_2 by Franks model which is a leaf gas-exchange proxy for CO_2 reconstruction (Franks et al., 2014; Maxbauer et al., 2014; Kowalczyk et al., 2018) that has been increasingly applied to a wide range of plant fossils through geological times (Tesfamichael et al., 2017; Kowalczyk et al., 2018; Londoño et al., 2018; Li et al., 2019; Milligan et al., 2019; Reichgelt et al., 2016, 2020; Zhou et al., 2020; Steinthorsdottir et al., 2021b) due to its well-vetted mechanistic model for plant carbon assimilation (Farquhar and Sharkey, 1982; Farquhar et al., 1989), integration of stomatal and carbon isotopic information (Konrad et al., 2008, 2017; Franks et al., 2014), and well-constrained CO_2 estimates at higher CO_2 levels without the requirement of fossil taxa with close modern equivalents (Royer et al., 2019; Konrad et al., 2020). In a recent study, several key Franks model parameters were further constrained and their sensitivities were tested in conifer taxa, including the two redwood genera used in this study, to enhance the model performance (Liang et al., 2022). To assess the potential of applying the modified cleared leaf epidermis method described in Liang et al. (2022) to common plant fossil compressions, we analyze leaf molecular composition of the two genera, representing both evergreen and deciduous habits with different tissue textures. By applying the recommendations of constrained parameterization outlined in Liang et al. (2022), we reconstruct early Miocene atmospheric CO_2 concentrations using these *Metasequoia* and *Sequoia* fossils. Recent comparisons between gas-exchange models and the traditional stomatal frequency (SF, including SD—stomatal density, SI—stomatal index, etc.) method on the same conifer fossils have revealed a systematic underprediction in the SF proxy, a phenomenon underpinned by similar theoretical framework (Konrad et al., 2020; Liang et al., 2022). We further examine this discrepancy by comparing our Franks model results with different SF-based results as well as previously-published CO_2 estimates by other proxies.

2. Materials and methods

2.1. Materials

Fossil leafy branches of two redwood genera, *Metasequoia* and *Sequoia* (Cupressaceae Gray, Christenhusz et al., 2011), were collected from the Hannuoba Formation (N*h*) in Erlongshan, Zhuozi County, Ulanqab City, south-central Inner Mongolia Autonomous Region in northern China (Fig. 1). The Hannuoba Formation was named after Hannuoba basalts which were originally discovered from and named after the location Hannuoba in Zhangjiakou City, Hebei Province, by George Brown Barbour in 1929 (Barbour, 1929; Wang et al., 1985). These basalts were subsequently found widely distributed in Hebei Province, Inner Mongolia, and northern Shanxi Province in northeastern China. K–Ar dating confirmed that basalts at the eastern area were formed by two major volcanic cycles, with the first cycle erupted ~24 Ma ago while the second ~18 Ma ago; thus, fluvial and lacustrine sedimentary layers that are interbedded within but mostly between these two cycles are early Miocene in age (Wang et al., 1985). This determination was further confirmed by additional K–Ar datings in the nearby Jining District, Ulanqab (~33–9.4 Ma, Zhang and Han, 2006) and Zuoyun County, Shanxi Province (~23.9–15.13 Ma, Li and Li, 2003). These radiometric dates are in broad agreement with vertebrate and plant fossils found in the area. A Miocene beaver *Monosaulax changpeiensis* C.K.Li was described from interbedded sediments of the Hannuoba basalts (Li, 1962). Abundant plant fossil compressions, dominated by *Acer*, *Alnus*, *Comptonia*, *Metasequoia*, *Platycladus*, *Sequoia*, and *Zelkova* were found in the fluvial-lacustrine phase of the deposit, and biostratigraphic correlations agreed with a Miocene age, highly likely in early Miocene between 19.35–22.83 Ma (He et al., 2018). Redwood fossils used in this paper were found in white mudstones, gray mudstones, and black oil shales associated with olivine and pyroxene basalts. Some of these fossils were used in Liang et al. (2022) to demonstrate the effectiveness of the cleared leaf epidermis technique and to obtain the Franks model parameters; but this study is the first time when detailed CO_2 reconstructions are conducted using these Inner Mongolian redwood fossils. All specimens are deposited at the Geological Museum at Chang'an University, Xi'an, China.

2.2. Methods

2.2.1. Fossil cleared leaf epidermis sample and clean cuticle sample preparation

In order to obtain complete stomatal apparatus structures for accurate measurements of guard cell length (GCL) and width (GCW),

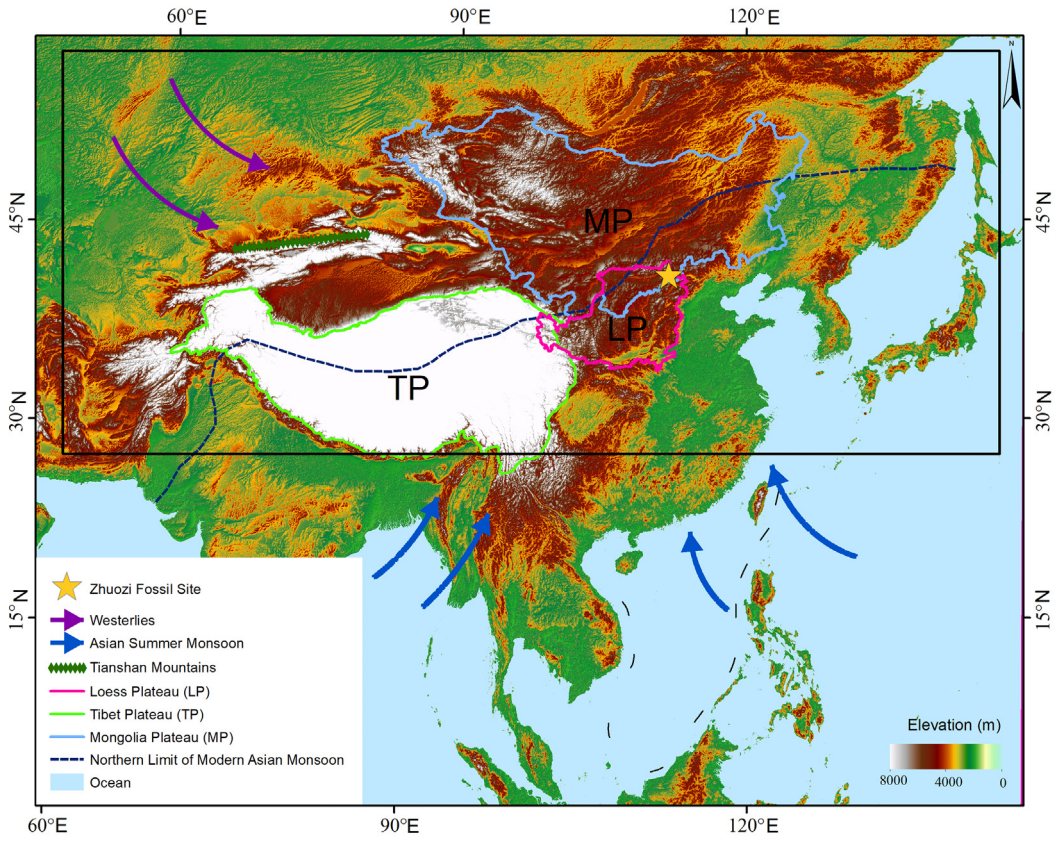

Fig. 1. Geographic map with modern topographic elevations showing the location of the Zhuozi fossil site (yellow star) relative to the Mongolian plateau (MP), the Loess plateau (LP), and the Tibetan plateau (TP). Dominant circulation systems—Asian summer monsoon (blue arrows), Westerlies (purple arrows), and the northern limit of modern Asian monsoon (dark blue dashed line)—were adopted from Yang et al. (2021). The cutoff area is further illustrated as a paleo-geographic reconstruction in Fig. 7.

parameters required for the Franks model, Liang et al. (2022) modified the conventional cleared leaf method. As it yields cleared leaf epidermises, we here propose to rename our previously described "modified cleared leaf method" in Liang et al. (2022) as "cleared leaf epidermis (CLE) method." Briefly, to remove the attached inorganic matrix, fossil leaf fragments taken from the middle ½ portion of a leaf located at the middle ½ portion of a branchlet were pretreated with 16% HCl and 40% HF. After being completely neutralized with deionized water (diH_2O), they were soaked in 70% HNO_3 for approximately 4–15 h depending upon the size and texture of the leaf fragments, to decolorize and oxidize mesophyll tissues. When the samples became clear (transparent) and light yellow in color, they were immediately neutralized with diH_2O and transferred to a microscope glass slide for the separation of the two epidermises by applying 0.4% NaClO for 5–10 s and using a fine dissecting needle (ideally an acupuncture needle used in traditional Chinese medicine) under a stereo microscope. While NaClO can further oxidize mesophyll tissues, it can also damage epidermal tissues if treated for too long; thus, the optimal timing of this step is critical. We thus recommend to first add 5 drops of diH_2O and then add 1 drop of 2% NaClO on the sample, giving full attention to the change under the dissecting microscope so that the reaction can be terminated promptly. When the two epidermises were separated, the loosened mesophyll tissues were washed away with diH_2O and the epidermises (with a certain amount of mesophyll tissues attached to ensure no or very little damage on epidermises) were stained with 1% Safranin O for less than 10 s to outline clearly-defined cell walls of the three dimensional (3D) epidermises, including stomatal complexes.

The mounted samples were observed and imaged using a Zeiss Primo Star light microscope fitted with a MicroPublisher RTV digital camera. By applying ImageJ 1.5a and CorelDRAW X8, we obtained whole leaf stomatal density (SD-WL) from a representative area spanning the half-leaf width, SI within a stomatal zone (only for *Metasequoia*), and GCL and GCW from 5–10 stomata with clearly-defined cell walls (Liang et al., 2022).

We also obtained clean cuticles from some samples using the traditional cuticle preparation method (Kerp, 1990; Wang and Leng, 2011; Wang et al., 2015) to verify the SI counting.

2.2.2. Organic geochemical analyses

Stable carbon isotope ($\delta^{13}C$) measurements of bulk-leaf samples at Texas A&M University Stable Isotope Geoscience Facility were performed following standard protocols (e.g., Yang et al., 2009; Liang et al., 2022). Determinations of $\delta^{13}C$ employed a Thermo Scientific DeltaPlusXP isotope ratio mass spectrometer coupled with a Carlo Erba NA 1500 Elemental Analyzer. Carbon isotopic composition is expressed in delta notation relative to the Vienna Pee Dee Belemnite standard (VPDB) in per mil (‰). Analytical precision was determined using two-point calibration obtained from USGS40 and 41a standards, within 0.20‰. Reproducibility was verified using internal standards as well as duplicates and replicate samples. Measurements from samples containing low carbon content (<35 wt% TOC or <0.4 μg) were excluded due to potential loss of organic carbon during taphonomic and diagenetic processes.

For pyrolysis-Gas Chromatography-Mass Spectrometry (Py-GC-MS) analysis, standard ultrasonication for 15 min with 2:1 (*v*/*v*) dichloromethane (DCM): methanol (MeOH) solvent was performed for organic extraction of free lipids from the leaf samples (Yang et al., 2005). Samples were then pyrolyzed at the Laboratory for Terrestrial Environments, Bryant University, using a CDS 5250 Pyroprobe by combusting the tissue to convert macromolecular compounds to GC amenable products. About 0.5–2 mg of powdered dry residue samples were sandwiched between pre-incubated (500 °C) glass wool inside a quartz

tube and inserted in the pyroprobe. The pyrolysis probe was set at 610 °C for 20 s in a helium gas flow. Compound detection and identification were performed using an Agilent 7890A GC System equipped with a Thermo TR-1 capillary column (60 m length, 0.25 mm i.d. and 0.25 μm film) coupled to a 5975C Series Mass Selective Detector (MSD). The GC oven was programmed from 40 °C (5 min hold) to 100 °C at 10 °C/min, then to 300 °C at 6 °C/min (25 min hold) with helium as the carrier gas. The MS source was operated at 250 °C with 70 eV ionization energy in the electron ionization (EI) mode and the MS Quadrupole mass analyzer was set to 150 °C with a scan rate of *m/z* 50–500. Compounds were identified by comparing their spectra with those reported in the literature (Ralph and Hatfield, 1991; Yang et al., 2005, 2007; Gupta et al., 2009; Witkowski et al., 2012). Duplicate analyses of each sample were conducted for analytical consistency.

2.2.3. Franks model and data parameterization

We applied the Franks model (Franks et al., 2014; Maxbauer et al., 2014; Kowalczyk et al., 2018) to estimate atmospheric CO_2 concentrations (c_a, ppm) as expressed in Equation 1:

$$c_a = \frac{A_n}{g_{c(tot)} \times (1 - c_i/c_a)} \quad (1)$$

where A_n is the standardized photosynthetic rate of leaf CO_2 assimilation, c_a is the atmospheric CO_2 concentration, c_i is the intra-leaf CO_2 concentration, and $g_{c(tot)}$ is the total leaf conductance.

For the photosynthetic rate (A), we followed the recommendation of Reichgelt and D'Andrea (2019) to apply the generic value (A_0) of the group. As different plant taxa, different habits (e.g., woody, herbaceous, etc.), and different habitats (such as different light conditions) can affect A_0, the most appropriate surrogate/generic value should be considered. For *Metasequoia* and *Sequoia*, we chose $A_0 = 10$ μmol m^{-2} s^{-1} (STDEV = 1.0), a conifer generic value originally recommended by Franks et al. (2014) and then by Reichgelt and D'Andrea (2019). The ratio c_i/c_a are inferred from carbon isotopic composition of plant fossils, but a systematic correction of 1‰ carbon isotope fractionation due to tissue decay during early diagenesis (Witkowski et al., 2022) was applied as recommended by Liang et al. (2022). For calculating $g_{c(tot)}$, we used three parameters based upon recommendations given in Liang et al. (2022): GCL, GCW, and SD-WL measured from the middle ½ portion of a leaf collected from the middle ½ portion of a branchlet. For other input parameters, we followed previous literature recommendations (Franks et al., 2014; Maxbauer et al., 2014; Royer et al., 2019; Liang et al., 2022). We ran the model using the R script of Franks model V2 (Kowalczyk et al., 2018; Royer et al., 2019) (See Supplementary Material Table S2 for detailed input parameters).

2.2.4. Stomatal index (SI) method for Metasequoia

Royer et al. (2001) established the relationship of c_a (shown as pCO_2 in Equation 2) and SI of modern species *Metasequoia glyptostroboides*:

$$\rho CO_2 = \frac{SI - 6.672}{0.003883 \times SI - 0.02897} \quad (2)$$

where SI is expressed in Equation 3 (Salisbury, 1928):

$$SI = \frac{\text{stomatal number}}{\text{stomatal number} + \text{epidermal number}} \times 100\% \quad (3)$$

For calculating SI, we used CorelDRAW X8 to draw the field-of-view (FOV) within a stomatal zone. The selected FOV should avoid the edge of the stomatal zone; preferably no less than 0.06 mm^2 (Liang et al., 2022) and ensure that all four sides pass through the middle of the farthest stomatal complex that can be reached by that side. Image J software was applied to calculate the numbers of stomata and the epidermal cells in the FOV. The results were compared with estimates based upon the application of calibration functions described in Beerling et al. (2009).

3. Results

3.1. Plant fossil systematic description

We follow the classification of extant gymnosperms of Christenhusz et al. (2011) at the family and genus levels. Unless stated otherwise, all leafy measurements were carried out at the middle ½ portion of a leaf located at the middle ½ portion of a branch and all branch measurements were performed at its middle ½ portion.

Family: Cupressaceae Gray, 1822

Genus: ***Metasequoia*** Hu & W.C. Cheng, 1948

Species: *Metasequoia* sp. (*M.* cf. *glyptostroboides* Hu & W.C. Cheng, 1948)

Locality: Erlongshan, Zhuozi County, Ulanqab City, Inner Mongolia Autonomous Region, China.

Holotype: ELS-19-148 (Fig. 2A, B, G, H, I, J).

Additional material: ELS-18-130 (Fig. 2C); ELS-19-345 (Fig. 2D, E); ELS-19-138 (Fig. 2F).

Stratigraphic horizon: Hannuoba Formation (N*h*).

Description: Twelve simple leafy branches (branchlets) were discovered. Branchlet axes are slender, 0.53–0.88 (median 0.78) mm thick. As none of the branchlets are completely preserved, their overall shape is unknown, but the most complete one (Sample ELS-19-148, see Fig. 2A and fig. 2A in Liang et al., 2022) shows an elliptic shape and bears ~20 pairs of leaves. Leaves are decussately arranged, with their bases twisted to form two oppositely paired ranks (Fig. 2A–F). Leaves are spaced sparsely to closely (~8–16 leaves per centimeter of the axis) with a wide range of diverging angles between 28–68°. Although both the density and diverging angles vary largely from branchlet to branchlet, they are more or less consistent within a single branchlet.

Leaf shape is linear. Leaves are 7.8–13.8 (12.0) mm long and 0.94–1.90 (1.2) mm wide, with length/width ratios (L/W) of 6.6:1–11.2:1 (8.3:1). Each leaf has an obvious midvein and two entire margins, which are parallel except for leaf base and apex. Leaf bases are rounded and twisted, appearing as with a very short petiole (Fig. 2E). Leaf apices are rounded to bluntly pointed or mucronate (Fig. 2E).

Most leaves that we observed are hypostomatous, with all stomata arranged in two obvious zones/bands aside from the midvein. The only exception was observed on sample ELS-19-148 which has a few stomata in the apical region of the adaxial surface (Fig. 2G). Both epidermises are covered with thin cuticles, with the abaxial one very thin and fragile.

The adaxial epidermis (Fig. 2G–H) has cells regularly arranged in longitudinal rows, elongated along the long axis of the leaf, with roughly rectangular outlines. The lateral cell anticlines are slightly undulate to straight. The polar anticlines are generally straight, oblique or at right angles to the lateral ones. The ordinary epidermal cells are 41.0–128.7 (70.7) μm long and 14.1–43.0 (21.1) μm wide, with L/W of 1.2:1–6.1:1 (3.1:1).

The abaxial epidermis has strongly uneven type cuticles (Fig. 2G–J and Fig. 3; refer to Leng et al., 2001; Leng, 2005; Wang, 2010; Wang et al., 2019 for detailed definition), particularly in the stomatal zones. In the three non-stomatal zones epidermal cells are similar in shape and size to those of the adaxial surface. The stomatal zones are 160.5–266.2 (226.8) μm wide. Ordinary epidermal cells in the stomatal zones have their outlines hardly distinguishable due to the strong outward bulges of their periclinal walls, due to the strongly uneven type. Stomata are irregularly located in the zone but oriented parallel to the long axis of the leaf (Fig. 2G–J). Two guard cells are sunken; each guard cell has an obvious lower, upper, and medial woody lamella (Fig. 3). The lamellae of two guard cells extend towards both ends to form two T-shaped polar lamellae, with a completely fused part forming

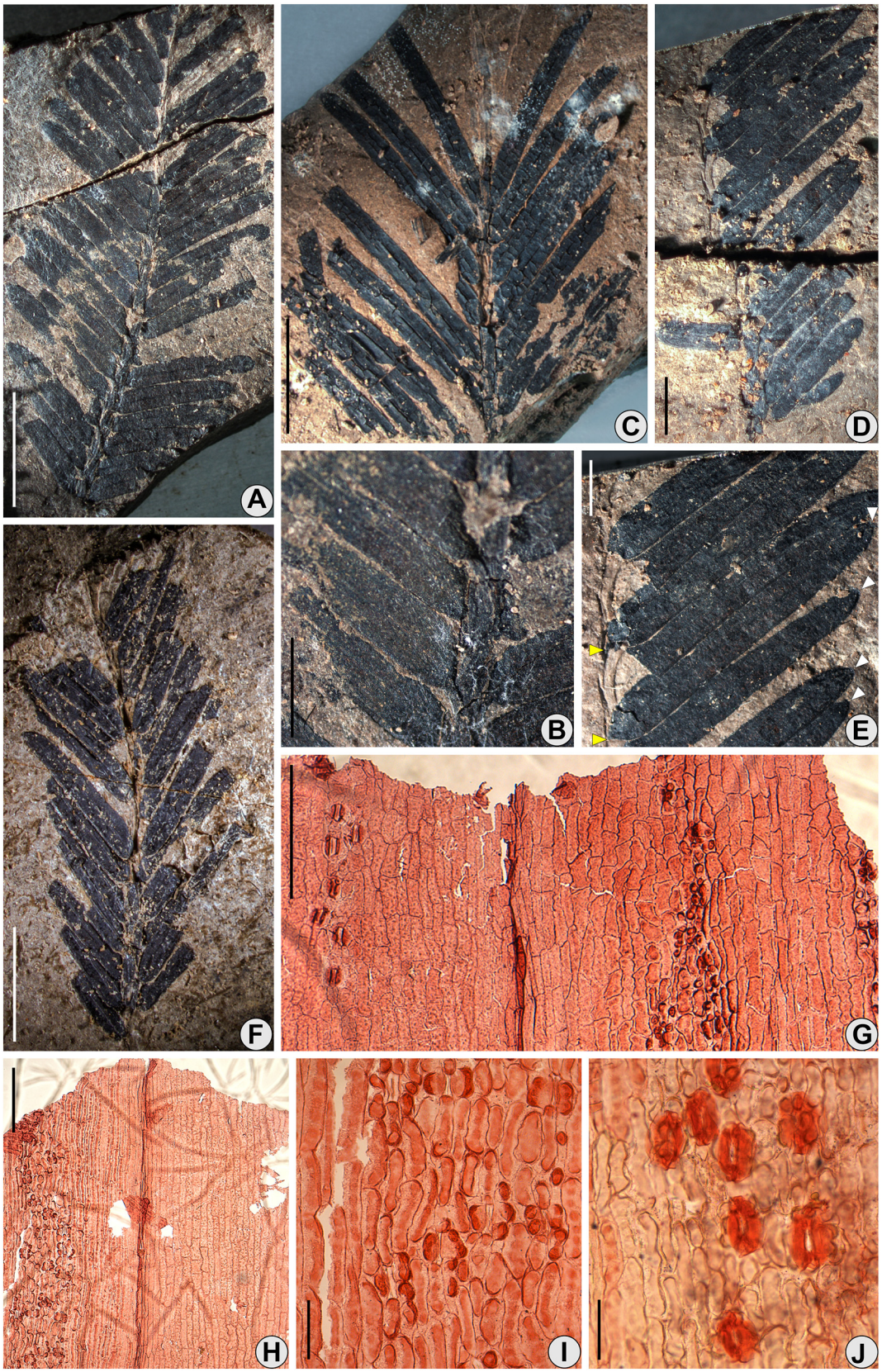

Fig. 2. Photographs showing gross morphology (A–F) and light microscope photographs showing micro-morphology of clean cuticles (G–I) and cleared leaf epidermis (J) of *Metasequoia* fossils. A: The most complete branchlet, sample ELS-19-148. B: Closer up of A, showing decussately arranged leaves. C: Sample ELS-18-130. D: Sample ELS-19-345. E: Closer up of D, showing rounded leaf bases with very short petioles (yellow triangles) and rounded to bluntly pointed or mucronate leaf apices (white triangles). F: Sample ELS-19-138. G: Adaxial (left) and abaxial (right) cuticles of the apex of a leaf located in the ½ middle portion of sample ELS-19-148. A few stomata are seen on the adaxial surface. H: Adaxial (right) and abaxial (left) cuticles of sample ELS-19-148. Stomatal zone is only seen on the abaxial surface. I: Stomatal zone on the abaxial surface of sample ELS-19-148, showing strongly uneven type of cuticle. J: Abaxial epidermis of sample ELS-19-148 showing strongly uneven type of cuticle and eight stomata. Samples in H–J are all from the ½ middle portion of a leaf located in the ½ middle portion of a branchlet. Scale bars: A, C, F = 10 mm; B, D, E = 5 mm; G, H = 200 μm; I, J = 50 μm.

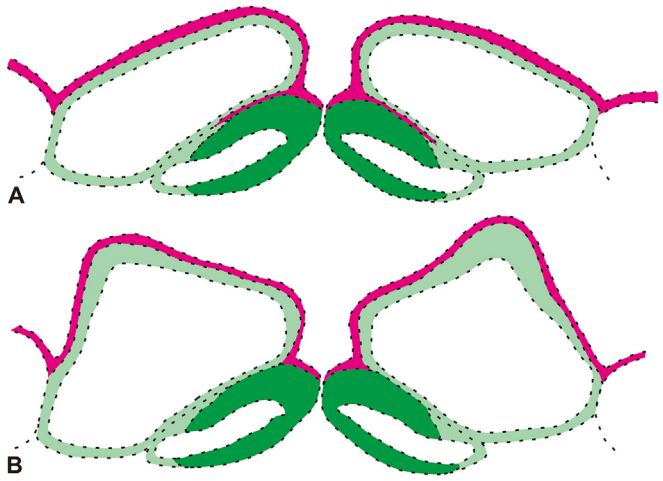

Fig. 3. Schematic drawings of transverse vertical sections of the abaxial epidermis through a stoma and its surrounding cells, illustrating two types of cuticles of *Metasequoia*: even (A, with flat epidermal cells) and uneven (B, with bulges on epidermal cells). Cuticular membranes are in pink, cellulose cell walls in light green, and woody lamella of the two guard cells (lignified parts of cell wall) are in dark green. The lower woody lamella is thinner but wider than the upper woody lamella. Sketched based on various light microscopic and SEM images taken in the Laboratory for Terrestrial Environments, Bryant University, images in Wang (2010), as well as Fig. DR7 in Maxbauer et al. (2014).

a "stem" (Refer to Fig. 3 and description in Liang et al., 2022). The two guard cells are surrounded by 4–6 overarching epidermal cells which are arranged in a unique way: two are located on the two polar sides while the remaining 2–4 are arranged along the sides almost in parallel (refer to Fig. 3 in Liang et al., 2022).

Comparison and remarks: Flat leafy branches and branchlets with dorsiventrally flattened linear and entire leaves arranged in two ranks are characteristic in five basal genera of Cupressaceae: the extinct *Yanliaoa* and the extant *Sequoia*, *Metasequoia*, *Taxodium*, and *Glyptostrobus* (Ma et al., 2021). Among them, *Metasequoia* can be readily identified by its decussate-turning-opposite phyllotaxy while other four genera have helical/spiral one. Thus, our samples can be undoubtedly assigned to *Metasequoia*.

The genus *Metasequoia* has been widely reported in the Northern Hemisphere since late Cretaceous (LePage et al., 2005). More than twenty fossil species have been proposed but due to their overlapping characteristics, most of them have been merged and currently only two are accepted widely: *M. occidentalis* (J.S.Newberry) Chaney and *M. milleri* G.W. Rothwell & Basinger which differ from each other and from the only living species *M. glyptostroboides* mainly in their cone morphology (Liu and Basinger, 2009; Wang et al., 2019). Our samples are all leafy branchlets, lacking reproductive organs and all observable gross morphological characteristics fall within the ranges of those of three species. However, the uneven type cuticles of our specimens confirm their closest affinity to the living species *M. glyptostroboides* as well as *Metasequoia* sp. (cf. *M. glyptostroboides*) reported from the middle Miocene of Zhenyuan, Yunnan, China (Wang et al., 2019). Our samples and the Zhenyuan samples are so far the only two fossil taxa possessing uneven cuticles. As a result, due to the lack of many other organs (such as trunk, compound branches, and reproductive organs) we follow Wang et al. (2019)'s treatment to tentatively use the Open Nomenclature (ON) qualifier sp. (abbreviation of "species", refer to Sigovini et al., 2016 for annotation) after the genus name to indicate the provisional status of the species level identification and add *M.* cf. *glyptostroboides* in parenthesis to indicate that all currently observed characteristics of branchlets, leaves, and leaf epidermises fall within the ranges of those of the living species. The abbreviation cf. is for "confer" (refer to Sigovini et al., 2016 for annotation), added before the species epithet rather than the generic name to indicate the species rather than genus level uncertainty.

Genus: ***Sequoia*** Endl., 1847

Species: *Sequoia* sp. (*S.* cf. *sempervirens* (D.Don) Endl., 1847)

Locality: Erlongshan, Zhuozi County, Ulanqab City, Inner Mongolia Autonomous Region, China.

Holotype: ELS-18-201 (Fig. 4A, B, G, H, I).

Additional material: ELS-19-87 (Fig. 4C, D, F); ELS-18-248 (Fig. 4E)

Stratigraphic horizon: Hannuoba Formation (N*h*).

Description: Six specimens containing eight leafy branches were discovered. Five are preserved as individual ultimate branches (thus branchlets) with their apical parts preserved but basal parts missing. One branch (Sample ELS-18-201, see Fig. 4A) has its base preserved but apical part missing, thus whether it is a branchlet or a compound shoot with more than one branching orders is unknown. Branch axes are slender to stout, 0.6–1.0 (0.7) mm thick. As none of the branches are completely preserved, their overall shape, length, and number of bearing leaves are unclear, with their width of 8.9–17.2 (12.9) mm. The shape of the only preserved base is cuneate and the shape of the apex is obtuse.

Leaves are alternately and spirally arranged, with their bases twisted to form two ranks (Fig. 4A–E). Leaves are spaced sparsely to closely. Although the full range of variation is unknown, ~9–15 leaves per centimeter have been measured. Leaves depart from the axes at angles of 17–60°. Although both the density and diverging angles vary largely from branch to branch, they are more or less consistent within a single branch.

Leaves are sessile, with their bases decurrent (Fig. 4D). Their apices are acute. Leaf shape is linear. They are 5.5–12.3 (8.4) mm long and 0.66–1.19 (0.8) mm wide, with L/W of 6.5:1–10.8:1 (8.5:1). Each leaf has an obvious midvein and two entire margins, which are parallel except for leaf base and apex.

Leaves are amphistomatous (Fig. 4F) although the existence of hypostomatous leaves cannot be completely excluded. All stomata are arranged in two obvious zones aside from the midvein.

From the sample (ELS-19-87) with both adaxial and abaxial epidermises obtained from the same leaf, it has been observed that the ordinary epidermal cells of the non-stomatal zones on both surfaces are similar in shape and size. They are regularly arranged in longitudinal rows, elongated along the long axis of the leaf, with roughly rectangular outlines and straight cell walls. The polar anticlines can be oblique or at right angles to the lateral ones. They are 57.1–207.0 (117.9) μm long and 6.3–18.4 (11.8) μm wide, with L/W of 3.4:1–15.4:1 (10.3:1).

The stomatal zones of the adaxial and abaxial surfaces are hardly distinguishable, generally differ only in width; the adaxial zones are generally narrower, 88.4 μm wide (measured from sample ELS-19-87) while the abaxial zones are 154.5–278.9 (236.6) μm wide (measured from five samples). Ordinary epidermal cells in the stomatal zones are quadrangular, mostly with rounded or pointed corners, 28.7–100.8 (48.5) μm long and 6.6–29.6 (13.6) μm wide, with L/W of 1:1–15.2:1 (4.2:1).

Stomata are irregularly located in the zone but oriented parallel to the long axis of the leaf (Fig. 4F–I). Compared with *Metasequoia*, the guard cells of this species are less sunken. Each guard cell has an obvious lower, upper, and medial woody lamella. The lamellae of two guard cells extend towards both ends to form two T-shaped polar lamellae, with a completely fused part forming a "stem." The stomata are round or oval, 49.0–57.0 (53.4) μm long and 27.3–38.1 (28.5) μm wide, with L/W of 1.4–1.9:1 (1.8:1). Each stoma is surrounded by 4–6 epidermal cells which are almost indistinguishable from other ordinary epidermal cells.

Comparison and remarks: Compared with the five basal Cupressaceous genera with flat branchlets bearing two-ranked linear leaves, the observed gross morphology of our samples show the most similar characteristics to *Yanliaoa* and *Sequoia*, particularly the obviously decurrent leaf bases. However, epidermal characteristics, particularly those of the stomatal zones are largely different between *Yanliaoa* and *Sequoia*. For example, *Yanliaoa* has short rectangular-polygonal ordinary epidermal cells (Tan et al., 2018) while those of *Sequoia* are much elongated (Ma and Li, 2002a, 2002b; Ma et al., 2005; Zhang et al., 2015;

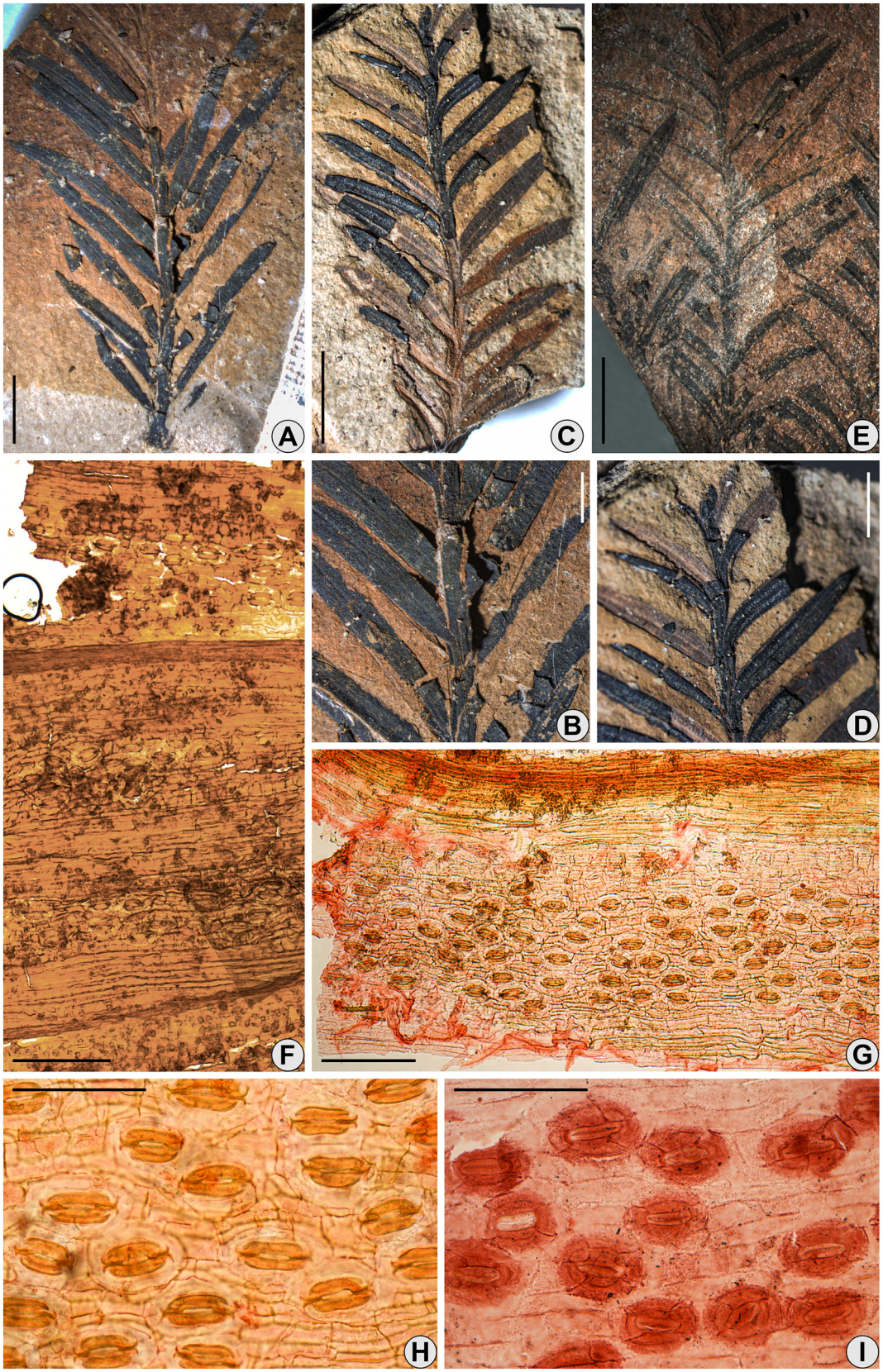

Fig. 4. Photographs showing gross morphology (A–E) and light microscope photographs showing micro-morphology of cleared leaf epidermises (F–H) and a clean cuticle (I) of *Sequoia* fossils. A: The only branch with a base (sample ELS-18-201). B: Closer up of A. C: Sample ELS-19-87. D. Closer up of C, showing sessile leaves with their bases decurrent and twisted. Leaves are alternately and spirally arranged. E. Sample ELS-18-248 showing the apical parts of three branchlets. F: Adaxial (upper) and abaxial (lower) epidermises of sample ELS-19-87 showing stomatal zones on both surfaces. G: Abaxial epidermis of sample ELS-18-201. H. Closer up of G showing stomata within the stomatal zone. I: Stomatal zone of the abaxial epidermis of sample ELS-18-201. Samples in F–I are all from the ½ middle portion of a leaf located in the ½ middle portion of a branch. Scale bars: A, C, E = 10 mm; B, D = 5 mm; F, G = 200 μm; H, I = 100 μm.

Ma et al., 2021). The epidermal characteristics of our sample are similar to those of *Sequoia*. Gross morphological characteristics of our samples also fall within the ranges of those of *Sequoia* (Fu et al., 1999; Ma and Li, 2002a, 2002b; Ma et al., 2005; Ma et al., 2021), confirming the identification to this genus.

Fossils of the genus *Sequoia* have been reported almost in every continent, with the oldest record dated back to the Jurassic (Chaney, 1950; Zhang et al., 2015; Ma et al., 2021). Most of the fossil species were established solely on gross morphological characteristics of leafy branches, some with cones' features added. However, most of these characteristics were later discovered overlapping among species, including the living representative *S. sempervirens*, making the species level identification solely on gross morphology difficult. In recent decades, several species have their micro-morphology of epidermis described in detail (Ma et al., 2005; Zhang et al., 2015; Ma et al., 2021), facilitating the more reliable identification.

All currently observed characteristics of our samples, including gross and micro-morphological ones, fall within the ranges of those of *S. sempervirens* (Fu et al., 1999; Ma and Li, 2002a, 2002b; this study) except that only linear leaves have been found from our samples while the living species possesses dimorphic leaves (linear and scale). However, our observation on living trees of *S. sempervirens* found that the existence of dimorphic leaves is complicated. Generally, most of the ultimate branchlets have only linear leaves while scale leaves can exist either along the main axis of a compound branch or at the base of some (not all) lateral branches of the compound branch. We have only one sample (ELS-18-201) showing branch base. It can be an ultimate branchlet containing only linear leaves; it can also be a non-ultimate lateral branch of a compound branch with only linear leaves, neither can completely exclude the existence of scale leaves on other branches that we have not discovered yet. Thus, the mono- or dimorphic leaves cannot against the affinity of our samples to the living species. However, as we only have characteristics of leafy branches, we tentatively use the ON qualifier sp. after the genus name *Sequoia* but add *S.* cf. *sempervirens* in parenthesis to indicate that all currently observed characteristics of branches, leaves, and leaf epidermises fall within the ranges of those of the living species.

3.2. Preservation of fossil leaf tissues

Fig. 5 illustrates the total ion chromatograms (TIC) generated by Py-GC-MS analyses of these fossil samples, indicating the relative intensity of detected compounds and their possible origins. The compound identification and inferred origins are listed in Table 1, where the peak numbers correspond to the numbers on the TIC diagrams (Fig. 5). Although the two genera produced slightly different pyrolysis products (pyrolysates), they yielded similar suites of compounds that are derived primarily from lignin. The only polysaccharide pyrolysate is 2-methyl-2-cyclopenten-1-one, a cellulose derivative that was detected in the *Sequoia* sample (Fig. 5A). All major pyrolysates, such as phenol, 2-methoxyphenol, 2-methoxy-5-methylphenol, and 4-ethenylphenol, are common lignin markers. The long retention time portion of the *Metasequoia* pyrogram is marked by traces of a homologous series of aliphatic *n*-alk-1-ene/alkane pairs (Fig. 5B). Compared with the pyrolysates of some extraordinarily preserved fossils, such as those from the Paleocene and Eocene sites of the Canadian Arctic and the middle Miocene site of Clarkia, ID, USA (Yang et al., 2005), the Zhuozi samples represent ordinary preservation of compression fossils with evidence of tissue decay.

3.3. Determination of key Franks model parameters

The CLE method allowed us to accurately measure key stomatal parameters in sunken stomata that the Franks model requires from fossil material. In *Metasequoia*, SD-WL ranges from 80.77 to 114.83 (average 93.26) stomata/mm^2, whereas SD-WL in *Sequoia* is 63.27–95.94 (80.77) stomata/mm^2 abaxially and 65.47 stomata/mm^2 adaxially, respectively. GCL is 37.31–50.59 (45.60) μm in *Metasequoia* and 49.04–57.02 (53.21) μm in *Sequoia*. GCW ranges 12.59–18.73 (15.33) μm in *Metasequoia* and 13.88–19.04 (15.65) μm in *Sequoia*. The mean SI value in *Metasequoia* is 12.81 (11.29–16.83)% (Table 2). Bulk-leaf $\delta^{13}C$ values range from −25.66 to −25.44‰ (average −25.56) in *Metasequoia* and −26.79 to −25.87‰ (−26.39) in *Sequoia* (Liang et al., 2022). Due to limited fossil compression material and tissue decay to satisfy required carbon contents (>35 wt%) (or >0.4 μg), some fossils did not yield reliable bulk-leaf $\delta^{13}C$ values, thus were excluded from Franks model applications. Detailed parameterization used for the Franks model to reconstruct early Miocene CO_2 using the two fossil species is summarized in Supplementary Material Table S2.

3.4. Reconstruction of early Miocene CO_2

The Franks model yielded mean c_a values of 423 ppm for *Metasequoia* (n = 3) (95% confidence interval 355–487 ppm) and 392 ppm for *Sequoia* (n = 3) (95% confidence interval 326–447 ppm), respectively (Table 2). Calculated SI values of *Metasequoia* range from 11.29% to 13.51%. Using the modern *Metasequoia* training curve established by Royer et al. (2001), the SI method yielded a mean CO_2 value of 296 ppm based on *Metasequoia* leaf fossils (n = 10) (standard deviation = 6). Applying the Beerling et al. (2009) algorithm, the same *Metasequoia* SI data produce a slightly higher mean value of 307 ppm (n = 10).

4. Discussion

4.1. Robust parameterization for the Franks model application

We obtained all required key input stomatal parameters from the two redwood species, including GCL, GCW, and SD-WL for calculating $g_{c(tot)}$, using the CLE method. While the previous study from our lab demonstrated the effectiveness of the method (Liang et al., 2022), here, we further explore the molecular preservation of the two redwood fossils by Py-GC-MS to elaborate and justify if the method can be applied to commonly preserved fossils to provide accurate parameters for the Franks model to reconstruct ancient CO_2 levels. For detailed parameterization, we followed the recommendations given in Liang et al. (2022) that are based upon studies of both modern and fossil cupressaceous leafy branchlets and by using the most updated version (V2) of the Frank model described in the Supporting Information of Kowalczyk et al. (2018).

Liang et al. (2022) showed that all stomatal parameters are relatively stable in the middle ½ portion of a needle located at the middle ½ portion of a branchlet, while bulk-leaf $\delta^{13}C$ values are relatively homogenous from various locations within a leaf and a branchlet. Thus, we prioritized all the middle portion of fossil samples for CLE treatment to obtain stomatal parameters and then used the remaining tissue for carbon isotope analysis. Accurate measurements of key stomatal parameters are more challenging for samples with uneven type cuticles which were reported as with "hollow papillae" (internal view) by Kerp (1990) or with "pronounced papillae" (external view) by Chaturvedi (1998). Leng et al. (2001) observed and described uncommonly large and dense "papillae" from most *M. glyptostroboides* leaves, and discovered, via SEM observations, that the so-called "papillae" are outward bulges caused by the underneath periclinal walls of the epidermal cells (Fig. 3; Leng et al., 2001; Fig. 2 in Liang et al., 2022), leading to the strong unevenness for the whole cuticular membrane.

The strongly uneven cuticle type has been found in the majority of *M. glyptostroboides* leaves, except for one living mature tree, the Paomu tree in Hunan, as well as in some sun leaves located at higher branches of living trees, and occasionally seedling leaves (Leng et al., 2001; Wang, 2010). Interestingly, the uneven type cuticle is not common in *Metasequoia* fossils, which are dominated by even type cuticle

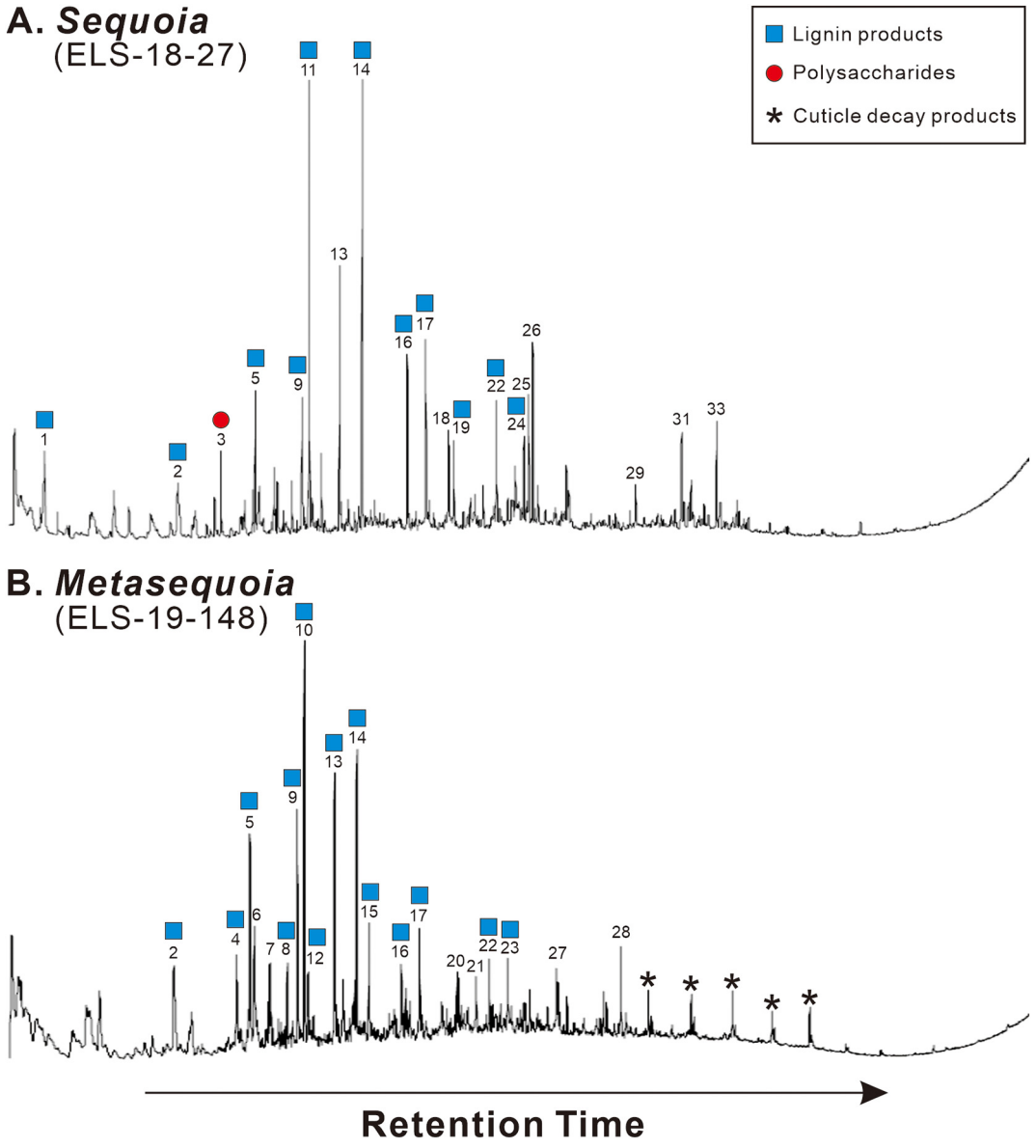

Fig. 5. Ion chromatograms of pyrolysates showing the relative intensity of the pyrolysis products (vertical axis) obtained from *Sequoia* (A) and *Metasequoia* (B) fossil leaf tissues. Compounds of different origins are marked with different symbols, and the numbers correspond to the MS identification provided in Table 1.

in almost all fossils so far found in hundreds of sites throughout the Northern Hemisphere since Cretaceous (LePage et al., 2005). Except for the Zhuozi site, the only uneven type fossil occurrence is from the middle Miocene Dajie Formation at Sanzhangtian Village, Zhenyuan County, Yunnan Province (Wang et al., 2019), where both even and uneven types are mixed, similar to the modern population. It remains an open question whether the two types of cuticle are due to evolutionary changes (due to genetic mutations) or related solely to physiological adaptations (light, water, temperature, etc.); but the presence of strongly uneven cuticle type in Zhuozi *Metasequoia* fossils indeed made the accurate measurements of guard cell dimensions and counting of epidermal cells a technical challenge. In addition, stomata of this genus are generally sunken deeply and their cell walls are partly and unevenly lignified to form obvious woody lamella (Fig. 3), which may have their width easily mistaken as guard cell width under a regular light microscope or an epifluorescence microscope (detailed description of the woody lamella and more images can be found from Liang et al., 2022). The combination of the uneven cuticle, sunken stomata, and woody lamella make the accurate measurements of guard cell dimensions and the precise determination of SI in *Metasequoia* leaves problematic, directly impacting on the accuracy of CO_2 reconstruction.

Fortunately, the CLE method and parameterization recommendations described in Liang et al. (2022) help circumvent these problems as illustrated with our redwood fossils. This CLE method accomplishes two objectives by obtaining an almost complete epidermis: (1) making the fossil leaf specimen transparent for SD-WL determination and SI calculations and (2) decaying most mesophyll tissues while maintaining the integrity for the epidermis for guard cell measurements. As epidermal cells generally have much thicker and sometimes lignified cell walls than mesophyll cells, distinguishing them can be accomplished by carefully controlling the timing of the bleaching processes. As the CLE method is a relatively milder treatment than clean cuticle preparation, it appears that the CLE method can be effective in obtaining relatively larger fragments from most fossil leaf compressions. Our study further confirmed that the CLE method can be applied to common fossils beyond extraordinarily-preserved fossil *Lagerstäten*.

The Py-GC-MS analysis shows signs of tissue decay in both Zhuozi redwood species, as most preserved biomolecules are decay-resistant

Table 1
Mass spectrometry (MS) identification of pyrolysis products of fossil *Metasequoia* and *Sequoia* samples. Peak numbers correspond to those in the chromatograms illustrated in Fig. 5. Compound names, characteristic fragment ions, and possible precursors are provided. Lg = lignin and Ps = polysaccharide.

Peak number	Retention time (min)	Compound name	Frag (m/z)	Origin
1	1.966	Urea	60, 78, 77	Lg
2	7.03	C2-benzene	91, 106, 105	Lg
2	7.05	C2-benzene	91, 106, 105	Lg
3	8.741	2-Methyl-2-cyclopenten-1-one	99, 55, 69	Ps
4	9.484	Benzene, 1-ethyl-3-methyl-	111, 126, 105	Lg
5	10.011	Phenol	94,66	Lg
5	10.074	Phenol	94, 66	Lg
6	10.188	Column contaminate	105,281,120	
7	10.789	Unknown	105,120,119	
8	11.47	Phenol, 3-methyl-	108,107,77	Lg
9	11.842	Phenol, 3-methyl-	107, 108, 77	Lg
9	11.888	phenol, 3-methyl-	107, 108, 78	Lg
10	12.128	2-methylphenol	109, 124	Lg
11	12.157	2 Methoxyphenol	107, 108, 77	Lg
12	12.277	C2-1,2-benzenediol	138, 123	Lg
13	13.312	Column contaminate	73,355,267	
13	13.333	Column contaminate	355,73,267	
14	14.176	2-Methoxy-5-methylphenol	138,123,95	Lg
14	14.188	2-Methoxy-5-methylphenol	138,123,95	Lg
15	14.663	4-Ethenylphenol (Vinyphenol)	120, 91	Lg
16	15.916	4-Ethyl-methoxyphenol	152,137	Lg
16	15.956	4-Ethyl-methoxyphenol	152,137	Lg
17	16.643	4-Ethyl-methoxyphenol	150,135	Lg
17	16.66	4-Ethyl-methoxyphenol	150,135	Lg
18	17.5	Unknown	177,107,81	
19	17.713	Benzenemethanol, α-ethyl-4-methoxy-	137,109,166	Lg
20	18.113	Unknown	55,83,69	
21	18.857	Unknown	156,141,155	
22	19.335	2-methoxy-4-(1-propenyl)phenol	164,149,77	Lg
22	19.361	2-methoxy-4-(1-propenyl)phenol	164,149,77	Lg
23	20.076	2-hydroxy-3-methyl-2-cyclopenten-1-one	55,83,69	Lg
24	20.419	2-Butenal,2-methyl-4-(2,6,6-trimethyl-1-cyclohexen-1-yl)-	191,95,121	Lg
25	20.608	Unknown	119,105,204	
26	20.774	Unknown	173,188,174	
27	21.993	Unknown	175, 55,83	
28	24.516	Unknown	56,69,57	
29	24.722	Unknown	184,169,153	
30	25.603	1-Hexadecanol-,2-Methyl	57,71,85	Lg
31	26.5	Unknown	95,121,149	
32	27.28	1-Hexadecanol-,2-Methyl	57,71,85	Lg

lignin (Table 1 and Fig. 5). Compared with some extraordinarily preserved fossils such as the Cenozoic conifers from Canadian Arctic islands and the middle Miocene Clarkia deposits (Yang et al., 2005, 2007), our Zhuozi fossils are of far lower preservational quality. Such lignin-dominated compression fossils are widely found in the plant fossil record, further sustaining the great potential for future application of the CLE method. Especially, as a deciduous conifer, *Metasequoia* has a thin and fragile cuticle (particularly on the abaxial surface with stomata), making it difficult to obtain large pieces of abaxial clean cuticles for stomatal counting (Wang and Leng, 2011). The CLE method allows the recovery of large fragments for both the calculation of SF values and accurate measurements of Franks model parameters.

Pore depth (PD) and pore length (PL) are the two parameters conventionally used to calculate stomatal conductance $g_{c(tot)}$, which is

Table 2
Summary of reconstructed CO_2 (ppm) for early Miocene Zhuozi redwoods in Inner Mongolia using different proxy methods (FOV = field-of-view, S# = stomatal number, E# = epidermal cell number, SI = stomatal index). The 95% confidence interval calculated for the Franks model is given in parentheses.

Metasequoia	Sample number	FOV (mm^2)	S#	E#	SI	CO_2 (ppm) (SI proxy—Royer)	CO_2 (ppm) (SI proxy—Beerling)	CO_2 (ppm) (Franks model)
	ELS-18-61	0.16	10	64	13.51	291	306	403 (347/465)
	ELS-18-181	0.04	9	62	12.68	296	307	416 (355/487)
	ELS-19-148	0.06	8	55	12.70	296	307	451 (385/527)
	ELS-18-62	0.10	24	164	12.77	296	307	
	ELS-18-151	0.11	16	120	11.76	305	310	
	ELS-19-014	0.10	16	120	11.76	305	309	
	ELS-19-32	0.05	8	52	13.33	292	306	
	ELS-19-108	0.12	14	110	11.29	311	312	
	ELS-19-138	0.04	9	61	12.86	295	307	
	ELS-19-345	0.04	7	46	13.21	293	306	
	Fossil mean					296	307	423 (355/487)
Sequoia								
	ELS-18-27							452 (379/541)
	ELS-18-201							381 (326/447)
	ELS-19-87							343 (296/400)
	Fossil mean							392 (326-447)

related to the opening size of a stoma. PD is generally scaled from GCW as it is impractical to measure PD from most leaf fossils directly. On the other hand, while PL is directly measurable from fossil leaves, we recently demonstrated that in comparison with GCL and GCW, the directly measured PL values contain large across-the-board variations, either due to natural variations of pore opening or measurement artifacts, leading to large uncertainties in Franks model output (Liang et al., 2022). Thus, we followed the recommendation made by Liang et al. (2022) to use GCL to scale PL in this study.

Liang et al. (2022) further constrained a high impactful conifer stomatal parameter, SD-WL, from fossil material. SD-WL can be measured from a representative area spanning the entire half-leaf width from the middle ½ portion of the needle leaf, or to obtain within a stomatal zone (SD-SZ) using the ratio of stomatal zone width to half-leaf width (Liang et al., 2022). We have tested these options in modern conifers and found that SD-WL estimated from a representative area can be pretty close to the true SD-WL, thus applying to our study. We believe that using the CLE method, the constraint of high impact parameters, and the correction of bulk-leaf carbon isotope values due to tissue decay made our application of the Franks model more robust.

4.2. Early Miocene atmospheric CO_2 level

Our Franks model CO_2 reconstruction using two Zhuozi redwood fossil species yielded similar CO_2 levels around 400 ppm, with mean values of 423 ppm (*Metasequoia*) and 392 ppm (*Sequoia*), respectively. These values are ~100 ppm higher than estimates obtained from a previously-established and widely-used inverse relationship between the partial pressure of atmospheric CO_2 and plant SI (Royer et al., 2001) and a revised calculation algorithm (Beerling et al., 2009) using the same Zhuozi *Metasequoia* fossils (Table 2). To compare our Zhuozi sample results with other published early Miocene CO_2 reconstructions within the time interval of 19.35–22.83 Ma during which the Zhuozi fossils belonged to, we computed median values of reported data within this timeframe (Fig. 6). Our Franks model reconstructions are comparable with moderate CO_2 levels reported by Zhang et al. (2013), Pagani et al. (2011), and Super et al. (2018). Our CO_2 values are higher than those of Kürschner et al. (2008), Sosdian et al. (2018), Greenop et al. (2019), and Cui et al. (2020), but lower than reports of Witkowski et al. (2018) and Steinthorsdottir et al. (2019) (Fig. 6). Two high CO_2 reconstructions (median of 600 to 1000 ppm) by Ekart (1999) and Tesfamichael et al. (2017) are not included in Fig. 6 due to their large range and uncertainties. Unlike the extensively-modeled climate during the Eocene to Oligocene transition and the middle Miocene warming, there is a lack of modeled CO_2 range proposed to sustain the higher-than-present-day temperatures estimated for the early Miocene. Nonetheless, it is generally accepted that the early Miocene CO_2 was higher than late Oligocene but lower than that of the middle Miocene level (Steinthorsdottir et al., 2021a); thus a modeled threshold CO_2 range between the levels of Oligocene and middle Miocene would serve as a bracket flanking the early Miocene values. Given our current understanding of the Earth climate sensitivity (Hansen et al., 2013), recent modeling works suggest that CO_2 levels up to 850 ppm are needed to support the estimated global mean surface temperatures during the middle Miocene (Burls et al., 2021); similarly, 345 ppm has been modeled as the upper limit threshold to maintain the Antarctic glaciation during the Oligocene–Miocene transition (Greenop et al., 2019). These estimates of CO_2 thresholds are in general agreement with early modeling results (Herold et al., 2012; Goldner et al., 2014; O'Brien et al., 2020), thus we use these ranges of CO_2 thresholds to bracket the levels of early Miocene CO_2 values (Fig. 6). Our Franks model results are at the lower side of these modeled CO_2 range and are in general agreement with models that require moderate CO_2 forcing as the primary boundary condition controlling the estimated global mean temperatures during early Miocene (Hansen et al., 2013; Burls et al., 2021).

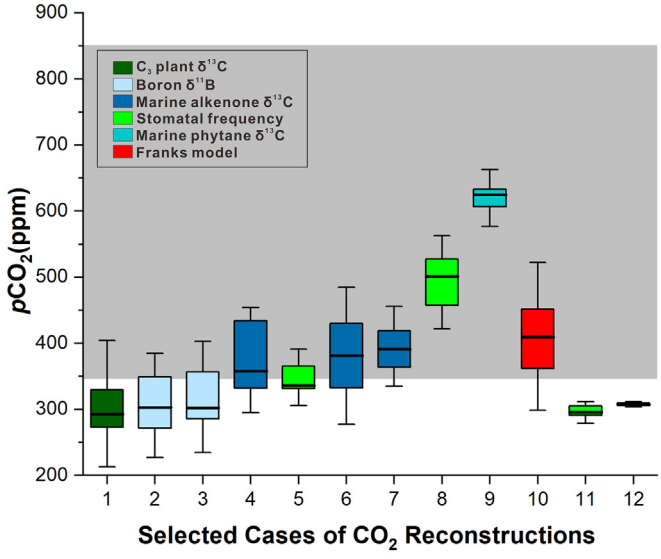

Fig. 6. Comparison of contemporary early Miocene (19.35–22.83 Ma) CO_2 reconstructions among previously published results (1–9, data extracted from https://paleo-co2.org/) and this study (10–12). 1. Cui et al. (2020); 2. Greenop et al. (2019); 3. Sosdian et al. (2018); 4. Zhang et al. (2013); 5. Kürschner et al. (2008); 6. Pagani et al. (2011); 7. Super et al. (2018); 8. Steinthorsdottir et al. (2019); 9. Witkowski et al. (2018); 10. This study by Franks model; 11. This study by Stomatal Index (SI) Royer et al. (2001) method; and 12. This study by Stomatal Index (SI) Beerling et al. (2009) method. Different colors code for different proxies; the shaded area indicates model required CO_2 range between late Oligocene (Greenop et al., 2019; O'Brien et al., 2020) and middle Miocene (Burls et al., 2021).

Early Miocene CO_2 reconstructions using the boron isotopes of planktonic foraminifera (Sosdian et al., 2018; Greenop et al., 2019) or the C_3 plant C isotope method (Cui et al., 2020) tend to produce relatively lower values than carbon isotope fractionations of alkenones (Pagani et al., 2011; Zhang et al., 2013; Super et al., 2018) or leaf-based reconstructions (Kürschner et al., 2008 and Franks model estimates of this study). Reconstructions using phytane from marine phytoplankton (Witkowski et al., 2018), terrestrial paleosols (Ekart, 1999), leaf SF method (Steinthorsdottir et al., 2019), and some Franks model estimates (Reichgelt et al., 2016; Tesfamichael et al., 2017; Londoño et al., 2018) have generated higher values for early Miocene. However, the current dis-congruency of early Miocene CO_2 reconstructions does not appear to be entirely stemmed from biases of different proxies as our Franks model results are consistent with marine alkenones method (Pagani et al., 2011; Zhang et al., 2013; Super et al., 2018) and in broad agreement with some leaf-based estimates (Kürschner et al., 2008). Both the terrestrial (Tesfamichael et al., 2017; Reichgelt et al., 2016) and marine (Sosdian et al., 2018; Westerhold et al., 2020) records have shown that CO_2 levels and global temperatures during the early Miocene have experienced a high level of fluctuations, sometimes during a relatively short geological interval (Tesfamichael et al., 2017). Thus, a large range of reconstructed CO_2 observed for the early Miocene may have been due to the wider stratigraphic distribution of these studied sites and the lack of a tighter chronological control for materials used for CO_2 reconstructions.

While the terrestrial-based proxies have their limitations, such as under predictions in the SF method (Konrad et al., 2020; Liang et al., 2022) or uncertainties and sensitivities of concentration of soil CO_2 that is contributed by soil respiration (Breecker, 2013), the marine-based proxies, while continuous, suffer from uncertainties in isotope fractionations and ocean temperature and chemistry (Sosdian et al., 2018; Super et al., 2018). Although an increasingly coherent picture of CO_2 changes during the Cenozoic started to emerge (Rae et al., 2021), the discrepancy seen in early Miocene CO_2 reconstructions highlights the need for additional data for improving calibrations and better

understanding assumptions and controlling factors underpinning the incongruent results among different proxies. Our detailed analysis of the systematic offsets observed between the Franks model and SI-based methods on *Metasequoia* fossils further illustrates this notion.

Previous Cenozoic CO_2 estimates using the *Metasequoia* SI proxy indicated that the SI method, including a revised algorithm described in Beerling et al. (2009), often produced relatively lower CO_2 values even with new statistical adjustments (Royer et al., 2001; Wang et al., 2015, 2020). For example, a level of ~300 ppm CO_2 was linked to the middle Miocene (Royer et al., 2001); preindustrial CO_2 levels of 270–280 ppm for late Pliocene and early Pleistocene (Wang et al., 2015); near present-day level CO_2 of 300–400 ppm reported for the middle Paleocene warming period (Wang et al., 2020). These *Metasequoia* SI-based estimates are at odds with the now well-documented Cenozoic CO_2 trend by multiple proxies during these periods (Foster et al., 2017; Sosdian et al., 2018; Steinthorsdottir et al., 2021a; Rae et al., 2021). Our current results further sustain this offset and show that SI-based *Metasequoia* estimates resulted in ~100 ppm lower values than that of the Franks model, a pattern that is similar to previous results obtained from recent studies of Franks model and SI reconstructions on *Metasequoia* leaves against measured modern CO_2 concentrations and known middle Miocene CO_2 levels (Kowalczyk et al., 2018; Steinthorsdottir et al., 2021b; Liang et al., 2022). It should be pointed out that the decay correction of the bulk-leaf $\delta^{13}C$ value in the positive direction would cause a lower value for the Frank model estimated CO_2, and thus is not responsible for the difference between leaf gas-exchange and SI estimates of CO_2.

The following reasons may have contributed to the discrepancy between the Franks model results and relatively lower CO_2 SI estimates using the same *Metasequoia* leaves. First, the formula fit of the inverse relationship between CO_2 concentrations and SI values in *Metasequoia* was originally established (Royer et al., 2001) and later refined (Doria et al., 2011) based upon herbarium specimens of short time interval (<100 years) under various natural CO_2 levels and young saplings grown in growth chambers with controlled CO_2. The curve may have approached its plateau level rapidly when CO_2 concentrations reach the upper 300 ppm levels, thus losing its sensitivity at higher CO_2 concentration—a common issue that almost all SF-based approaches have faced. Previous research has shown that stomatal development and distribution in *Metasequoia* seedlings and young saplings may differ largely from adult trees (Wang, 2010). Young plants in rapidly-changed and elevated CO_2 environments may behave differently from natural growing trees, as shown in *Ginkgo biloba* leaves (Barclay and Wing, 2016), causing inaccuracy and increased uncertainties in establishing training sets. Second, the uneven type of modern *Metasequoia* cuticles, based upon which the original curve was calculated, is notorious for its difficulties in accurately counting the number of epidermal cells due to (1) thin anticlinal cell walls and (2) irregular bulging of their periclinal wall (epidermal cells may have one to up to four bulges, see Leng et al., 2001; Liang et al., 2022). Each apparent bulge can be easily misrecognized as an epidermal cell, thus over counting the number of epidermal cells; as a result, artificially decreasing SI values in the training set calculation, resulting in the underestimation of CO_2 levels for fossil applications. Furthermore, except for this study, previously reported fossil *Metasequoia* are almost exclusively even type (but see Wang et al., 2019 for mixed types), increasing uncertainties regarding the accuracy of the formula established solely based upon uneven type cuticles. Third, our measurements of stomatal and epidermal cells of the Zhuozi *Metasequoia* based upon the CLE method yielded SI values approaching and exceeding the upper limit of the Royer et al. (2001) curve; thus, the extrapolation reduced the accuracy of its reconstructed CO_2 levels. In addition, Liang et al. (2022) has shown detailed statistical data regarding the non-uniformed distribution of stomata along an individual needle leaf in conifer species, including *Metasequoia*, and such variations in SI values along a leaf blade may have also contributed to the inconsistency of CO_2 estimates. In sum, the above reasons made the *Metasequoia* SI method, both its original curve fit and its fossil applications, largely prone to user-dependency biases.

Our application of a revised SI algorithm described in Beerling et al. (2009) to Zhuozi *Metasequoia* fossils yields slightly higher CO_2 concentrations (median value of 307 ppm) than the Royer et al. (2001) method, a pattern that is consistent with previous observations (Liang et al., 2022). Although case studies have reported congruent CO_2 estimates between the Franks model and SF proxies (Maxbauer et al., 2014; Li et al., 2019; Steinthorsdottir et al., 2021b), a recent comparative analysis of plant leaf-based proxies by Konrad et al. (2020) provided a theoretical framework for the systematic underprediction of CO_2 reconstructions using SF proxies; these underpredictions are biggest in warm and moist climates. It remains to be further explored whether this phenomenon of underprediction in SF method is unique to *Metasequoia* or has general implications across wider spectra of plant taxa.

In comparison with SF proxies which are largely based upon empirical data fitting and user-dependency in counting epidermal cells, we believe that the Franks model gives more consistent, robust, and stable ancient CO_2 estimates, as shown in recent studies (Reichgelt et al., 2016, 2020; Londoño et al., 2018; Steinthorsdottir et al., 2019, 2021a; Liang et al., 2022), due to its well-constrained parameters and dynamic incorporation of stomatal conductance, photosynthesis rates, and levels of gas-exchange (Franks et al., 2014; Royer et al., 2019; Liang et al., 2022). The systematic underestimation of CO_2 levels by the *Metasequoia* SI method points toward the need to reevaluate and/or systematically correct previous CO_2 estimates obtained exclusively based upon the application of SI method on *Metasequoia* fossils.

4.3. Early Miocene paleoclimate in relation to the Mongolian plateau

Both gross morphologies and cuticular characteristics of these redwood fossils from Inner Mongolia allow us to unambiguously assign them to *Metasequoia* and *Sequoia*. Under each genus, compared with all described species, both fossil and living, our fossils most closely resemble their sole living representative, *Metasequoia glyptostroboides* and *Sequoia sempervirens*, than any other fossil species. The close affinities between the two fossil species and their endemic modern living representatives give us the confidence to use them for paleoclimate and paleogeographic inference effectively. The occurrence of these early Miocene redwoods in Inner Mongolia is consistent with a relatively low elevation for the Mongolian plateau and a weak or an absence of monsoonal climate at the southeastern margin of the Mongolian plateau during the early Miocene.

The small living population of native *M. glyptostroboides* now only survives in the well-drained wet montane river and stream valleys in Hubei, Hunan, and Chongqing in south-central China (Leng et al., 2007; Zhao et al., 2020); similarly, living *S. sempervirens* populations are restricted in foggy coastal areas of southern Oregon and northern California in the USA (Noss, 2000; Johnstonea and Dawson, 2010)—both areas are characterized by winter and early spring wet conditions that are required for seed germination and foliation (Zhang et al., 2015; Wang et al., 2019). Recent observations of *M. glyptostroboides* seedlings grown under controlled greenhouse experiments clearly indicate that moisture conditions are critical to the control of seed germination as well as root development, stem elongation, and leaf growth in seedlings, thus directly contributing to the survivability of the species in the wild (Fan et al., 2020). Similarly, for *S. sempervirens* the germination of seeds and the survival of new seedlings require moist soil conditions during winter (Olson et al., 1990). One of the hallmarks of the Asian monsoon climate is its uneven distribution of precipitation concentrated in the summer and early fall (May through October) with an increasing dry winter and spring (Sun and Wang, 2005; Chiang et al., 2020), conditions that are detrimental to the survival of *Metasequoia* and *Sequoia*. These experimental data and field observations, along with the paleogeographic distribution of extensive fossil records of

Metasequoia and *Sequoia* led to the conclusion that the post-Miocene disappearance of these winter/spring moisture depended genera in most parts of China was due to a strong influence of monsoonal climate (Wang et al., 2019; Zhang et al., 2015). Given the co-occurrence of both genera in Zhuozi, along with the general characteristics of the whole flora (He et al., 2018), we infer that the early Miocene climate in eastern Mongolia and northeastern China was dominated by warm temperate climate with wet winter and early spring that nurtured the growth of these two redwood species. Thus, the lack of profound signatures of wet summer climate, characteristics of EASM, in Inner Mongolia implies either a weaker EASM beyond its northern limit or a total absence of monsoonal climate in the area during early Miocene.

The timing of the uplift of the Mongolian plateau in coordination with the rise of the northern Tibetan plateau and their role in the history of Asian climate changes has been an issue bearing great interest to paleoclimatologists and paleogeographers alike. Modeling work suggests that the uplifted Mongolian plateau influenced the strength of modern EASM by increasing the winter Westerlies in northern East Asia, especially when it combined with the uplift of northern Tibet and the Tianshan Mountains (Tang et al., 2013; Zhang et al., 2017; Sun and Liu, 2018). Recent modeling experiments also show that due to its geographic location, the Mongolian plateau can exert two times of impact on atmospheric effect than the Tibetan plateau on winter stratospheric circulations if it rose to a significant altitude (Shi et al., 2015; White et al., 2018). Further modeling work using modern climate data indicates that the change of the westerly jet of mid-tropospheric wind direction, which is influenced by the topography of the Mongolian plateau, is a major environmental forcing to control summer precipitation in northeastern China (Sampe and Xie, 2010); the interplay between middle latitudinal Westerlies and the EASM had an anti-phase relationship during the Pleistocene and Holocene (An et al., 2012; Chen et al., 2019). Thus, key questions need to be answered are whether a high Mongolian plateau existed and where were the possible sources of winter to early spring moisture that sustained the growth of these redwood species in Inner Mongolia during the early Miocene.

While proposals have suggested that the uplift of the southern Mongolian plateau (Hangay and east Sayan) began by the early Oligocene (Jolivet et al., 2007; Caves et al., 2014; Thumma, 2016), others argued that due to the continuation of India–Asia collision, the uplift of the major portion of the south Tianshan Mountains and Mongolian plateau occurred much later at ~6–5 Ma ago (Vassallo et al., 2007; Sun et al., 2009; Zhang and Sun, 2011). If an uplifted Mongolian plateau with significantly high elevations existed north of the Zhuozi fossil site, it would have largely weakened the Westerlies but enhanced the overall annual precipitation in northern China, leading to the increase of seasonality of precipitation in the current Inner Mongolia like much of the Holocene (Sha et al., 2015; Chiang et al., 2020). Similar to today's climate pattern in northern China, the compounded effects would have intensified anomalous summer low-level Southerlies and expanded the monsoon domain on the southeastern side of the Mongolian plateau (Zhang et al., 2017; Yu et al., 2018). However, the mild and wet winter–spring climate indicated by *Metasequoia* and *Sequoia* in early Miocene Inner Mongolia would suggest the opposite: The absence of high elevation topographic feature north of the fossil site.

A low terrain scenario for the Mongolian plateau during the early Miocene is also consistent with a strong westerly jet that increased dust deposits at the Chinese loess plateau at the same time (Guo et al., 2002, 2008) and delivered moisture from the Paratethys sea with strong penetration to northeastern China (Chen et al., 2019; Chen et al., 2020). Recent studies have shown that Westerlies have been a dominant source of moisture for Asia, especially on the Mongolian plateau, since the Eocene time (Caves et al., 2014). Currently, combined moisture brought by the EASM and the mid-latitude Westerlies contributes a significant portion of annual precipitation in eastern Mongolia and northeastern China (Piao et al., 2018). During a so-called Westerlies-dominated climatic regime, such as the Little Ice Age, much precipitation occurred in eastern Mongolia and northeastern China during fall and winter times with moisture transported by the Westerlies that were linked to sea surface temperature anomalies in the North Atlantic (Chen et al., 2019; Chen et al., 2020). Although the epicontinental Paratethys sea in the present-day Kazakhstan and Uzbekistan to west of Tibet and Tianshan Mountains areas has reduced its size from Eocene and Oligocene times, it remained to be a significant source of moisture for the Westerlies during much of Miocene time (Steininger and Rögl, 1984; Caves et al., 2014; Barbolini et al., 2020; Palcu et al., 2021). Liu et al. (2011) identified a general trend of wet conditions during early

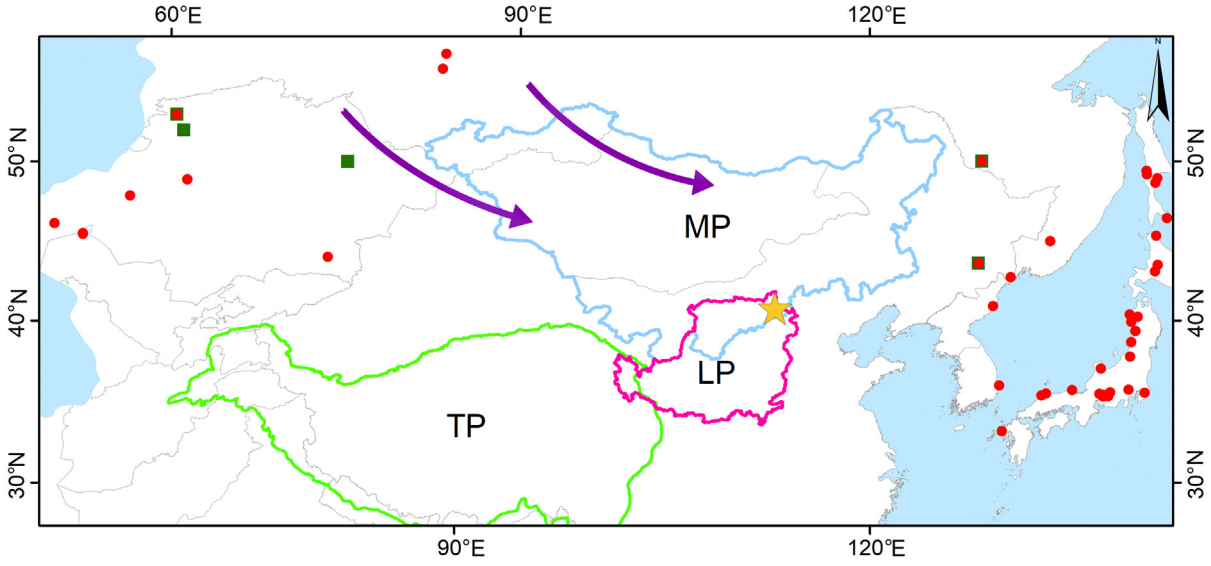

Fig. 7. Sketch map outlining major paleogeographic features (adopted from Steininger and Rögl, 1984 and Barbolini et al., 2020) in eastern Asia, including Mongolia and northeastern China (see the cutoff area in Fig. 1; ocean in blue; continent in white) with strong and displaced Westerlies (purple arrows) over the low land of Mongolia during early Miocene. The location of the Zhuozi fossil site (yellow star) is relative to a high elevation Tibetan plateau (TP) but low altitude Mongolian plateau (MP). LP = Loess Plateau. Notice the eastern tip of the Paratethys sea at the left of the map. Early Miocene *Metasequoia* (red circles) and *Sequoia* (green square) fossil localities are based upon Yang and Jin (2000), LePage et al. (2005), and Zhang et al. (2015).

to middle Miocene in northern China based upon reconstruction and comparison of mean annual precipitation in northern China but could not distinguish the seasonal distribution of the estimated total amount of annual precipitation. We argue that given the survival requirements for *Metasequoia* and *Sequoia*, most of the annual rainfall during the early Miocene may have occurred during winter and spring, along with the strong Westerlies. The extensive early Miocene distribution of *Metasequoia* and *Sequoia* in Asia also supports such an interpretation. The early Miocene Qiuligou flora in Jilin Province, northeast of Zhuozi, includes both *Metasequoia* and *Sequoia* (Li and Yang, 1984). The Zhuozi site marks the south-most fossil distribution for the two redwoods during the early Miocene. Toward the west, *Metasequoia* and *Sequoia* were found in middle latitudes of central Asia; toward the east, abundant *Metasequoia* fossils occurred east of the Mongolian plateau in eastern China, Japan, and eastern Russia, including the Sakhalin Island, in the pathway and under the influence of moisture delivered by the Westerlies (Fig. 7).

The Tibetan plateau has experienced progressive uplifts during Cenozoic and its major blocks have reached significant heights by the early Miocene (Wang et al., 2014; Ding et al., 2017; Spicer et al., 2021). However, without a high elevation of Mongolian plateau to the north, the tilted Westerlies were able to penetrate southward in eastern China to mute the EASM at its northern front; and as a result, to shift precipitation from summer to winter times (Fig. 7).

In summary, the occurrence of *Metasequoia* and *Sequoia* in Zhuozi, Inner Mongolia, during the early Miocene indicates a warm temperate climate with a mild and wet winter and early spring growing season. Given the early Miocene CO_2 level similar to but temperature higher than the present day (Burls et al., 2021; Steinthorsdottir et al., 2021a), in contrary to the model prediction of enhanced EASM (Li et al., 2019; Miao et al., 2020), the lack of EASM influence in eastern Mongolia and northeastern China during early Miocene can be attributed to the significant regional topographic effort (Farnsworth et al., 2019), including a relatively low paleoelevation for the present-day Mongolian plateau and Tianshan Mountains to the north and eastern-ward extension of the Paratethys sea to the west. Such type of Westerlies-dominated climate is consistent with the notion that the rise of the plateau with associated shift of moisture sources from Westerlies to monsoon-dominated climate sometimes along with the vegetation change occurred after the early Miocene. Such a scenario is congruent with paleoclimate evidence derived from plant fossil data from eastern China (Liu et al., 2011), especially the distribution of *Metasequoia* and *Sequoia* (Yang and Jin, 2000; LePage et al., 2005; Zhang et al., 2015), and reconciles extensive early Miocene eolian deposits (Guo et al., 2002, 2008) and late Miocene strengthening of EASM (An et al., 2001, 2015), as observed at the Chinese loess plateau.

5. Conclusions

Based upon the analysis of co-occurring *Metasequoia* and *Sequoia* from the early Miocene Hannuoba Formation at Zhuozi County in China's Inner Mongolia at the southeastern margin of the current Mongolian plateau, we conclude the following:

1. We reported the first occurrence of *Metasequoia* fossils that are solely represented by the strongly uneven type cuticles. The CLE method previously described by Liang et al. (2022) solved the problem of accurately counting the number of epidermal cells and measuring stomatal dimensions for uneven type cuticles. Based upon molecular analysis of fossil leaf tissues, we demonstrated that the CLE method can be readily applied to regular fossil compressions of both deciduous and evergreen conifer leaves for accurate measurements of epidermis that are used for both the Franks model and SF methods.

2. Applying the Franks model, we estimated mean CO_2 level for the early Miocene as 432 ppm (95% confidence interval 355–487 ppm) and 392 ppm (95% confidence interval 326–447 ppm) using fossil *Metasequoia* (n = 3) and fossil *Sequoia* (n = 3), respectively. These values are ~100 ppm higher than that obtained from the SI method based on the same *Metasequoia* leaf fossils (n = 10) by applying the modern *Metasequoia* training curve established by Royer et al. (2001) and modified algorithm of Beerling et al. (2009).

3. Our results explained and reconciled previous underestimates of Cenozoic CO_2 levels using the *Metasequoia* SI approach; and together with recent results from Liang et al. (2022) using modern and middle Miocene *Metasequoia*, our study revealed a consistent and systematic underestimation, positing that previous SI-based *Metasequoia* CO_2 reconstructions may be ~100–150 ppm lower than the target level.

4. The occurrence of both *Metasequoia* and *Sequoia* at the southeastern margin of the Mongolian plateau during the early Miocene strongly suggests a weak or absence of Eastern Asian summer monsoon in the region where the Mongolian plateau has not reached to significant altitudes. The winter–spring moisture required by the survival of these redwood seedlings was highly likely delivered from the Paratethys sea by the Westerlies over the Mongolian terrain with relatively low paleo-elevations.

Future research in the area would benefit from a more precise age determination of the fossil flora, perhaps based upon radiometric dating of the interbedded basalts directly associated with the fossil flora. Franks model reconstructions of ancient CO_2 using more diverse fossil species from the flora may improve calibrations. In addition, more modeling work is needed to explore CO_2 forcing for estimated global mean surface temperature during the early Miocene. The measured mean annual value of global CO_2 concentration in 2021 has reached to 416 ppm, the highest throughout the entire history of humanity and remarkably similar to what we reconstructed for the early Miocene in this study. The rapid annual mean rate of growth of CO_2 seen in the past few years, if not effectively mitigated, projects near future CO_2 level reaching to the middle Miocene level with global temperatures 5–7 °C higher. Thus, a better understanding of the pace and coupled temperature changes from early to middle Miocene would provide much needed scientific information for the prediction of near future global climate change and its consequences.

Declaration of Competing Interest

The authors declare that they have no known competing financial interests or personal relationships that could have appeared to influence the work reported in this paper.

Acknowledgements

We thank Li Wang (Xishuangbanna Tropical Botanical Garden), Chris Maupin (Texas A&M University), Kevin Burke and Katelyn Howard (Bryant University) for laboratory assistance and anonymous reviewers for their comments and suggestions to help improve the quality of the manuscript. The project was supported by Bryant University Summer Research Award (QL) and Charles J. Smiley Research Endowment (HY). LX was supported by the National Natural Science Foundation of China (No. 41872017) and the Foundation of State Key Laboratory of Palaeobiology and Stratigraphy (Nanjing Institute of Geology and Palaeontology, CAS) (No. 183125). This publication is dedicated to Professor Zhiyan Zhou's 90th birthday, honoring his monumental contributions to paleobotany. As Prof. Zhou's Ph.D. student, QL was inspired by his passion for fossil gymnosperms, including the two redwoods studied here. As a mentor, what Prof Zhou taught their students, ranging from detail-oriented scientific investigations to the ethic and responsibility of a scientist, benefited the rest of their scientific careers.

Appendix A. Supplementary data

Supplementary data to this article can be found online at https://doi.org/10.1016/j.revpalbo.2022.104743.

References

An, Z.-S., Kutzbach, J.E., Prell, W.L., Porter, S.C., 2001. Evolution of Asian monsoons and phased uplift of the Himalaya-Tibetan plateau since late Miocene times. Nature 411, 62–66.

An, Z.-S., Huang, Y.-S., Liu, W.-G., Guo, Z.-T., Clemens, S., Li, L., Prell, W., Ning, Y.-F., Cai, Y.-J., Zhou, W.-J., Lin, B.-H., Zhang, Q.-L., Cao, Y.-N., Qiang, X.-K., Chang, H., Wu, Z.-K., 2005. Multiple expansions of C4 plant biomass in East Asia since 7 Ma coupled with strengthened monsoon circulation. Geology 33, 705–708.

An, Z.-S., Colman, S.M., Zhou, W.-J., Li, X.-Q., Brown, E.T., Jull, A.J.T., Cai, Y.-J., Huang, Y.-S., Lu, X.-F., Chang, H., Song, Y.-G., Sun, Y.-B., Xu, H., Liu, W.-G., Jin, Z.-D., Liu, X.-D., Cheng, P., Liu, Y., Ai, L., Li, X.-Z., Liu, X.-J., Yan, L.-B., Shi, Z.-G., Wang, X.-L., Wu, F., Qiang, X.-K., Dong, J.-B., Lu, F.-Y., Xu, X.-W., 2012. Interplay between the Westerlies and Asian monsoon recorded in Lake Qinghai sediments since 32 ka. Scient.Rep. 2 Article number: 619.

An, Z., Wu, G., Li, J., Sun, Y., Liu, Y., Zhou, W., Cai, Y., Duan, A., Li, L., Mao, J., Cheng, H., Shi, Z., Tan, L., Yan, H., Ao, H., Chang, H., Feng, J., 2015. Global monsoon dynamics and climate change. Annu. Rev. Earth Planet. Sci. 43, 29–77.

Barbolini, N., Woutersen, A., Dupont-Nivet, G., Silvestro, D., Tardif, D., Coster, P., Meijer, N., Chang, C., Zhang, H.-X., Licht, A., Rydin, C., Koutsodendris, A., Han, F., Rohrmann, A., Liu, X.-J., Zhang, Y., Donnadieu, Y., Fluteau, F., Ladant, J.-B., Le Hir, G., Hoorn, C., 2020. Cenozoic evolution of the steppe-desert biome in Central Asia. Sci. Adv. 6 Article number: eabb8227.

Barbour, G., 1929. The geology of the Kalgan Area. Mem. Geol. Surv. China (A) 6, 54–61.

Barclay, R.S., Wing, S.L., 2016. Improving the Ginkgo CO_2 barometer: implications for the early Cenozoic atmosphere. Earth Planet. Sci. Lett. 439, 158–171.

Beerling, D.J., Fox, A., Anderson, C.W., 2009. Quantitative uncertainty analyses of ancient atmospheric CO_2 estimates for fossil leaves. Am. J. Sci. 309, 349–354.

Breecker, D.O., 2013. Quantifying and understanding the uncertainty of atmospheric CO_2 concentrations determined from calcic paleosols. Geochem. Geophys. Geosyst. 14, 3210–3220.

Burke, K.D., Williams, J.W., Chandler, M.A., Haywood, A.M., Lunt, D.J., Otto-Bliesner, B.L., 2018. Pliocene and Eocene provide best analogs for near-future climates. Proc. Natl. Acad. Sci. 115, 13288–13293.

Burls, N.J., Bradshaw, C.D., De Boer, A.M., Herold, N., Huber, M., Pound, M., Donnadieu, Y., Farnsworth, A., Frigola, A., Gasson, E., von der Heydt, A.S., Hutchinson, D.K., Knorr, G., Lawrence, K.T., Lear, C.H., Li, X., Lohmann, G., Lunt, D.J., Marzocchi, A., Prange, M., Riihimaki, C.A., Sarr, A.-C., Siler, N., Zhang, Z., 2021. Simulating Miocene warmth: insights from an opportunistic Multi-model ensemble (MioMIP1). Paleoceanogr. Paleoclimatol. 36 Article number: e2020PA004054.

Caves, J.K., Sjostrom, D.J., Mix, H.T., Winnick, M.J., Chamberlain, C.P., 2014. Stable isotope constraints on aridity in northern Central Asia and implications for the uplift history of the Altai and Hangay. Am. J. Sci. 314, 1171–1201.

Chaney, R.W., 1950. A revision of fossil *Sequoia* and *Taxodium* in western North America based on the recent discovery of *Metasequoia*. Trans. Am. Philos. Soc. 40, 171–263.

Chaturvedi, S., 1998. Micromorphology and vegetative anatomy of Taxodiaceae L. Geophytology 26, 43–56.

Chen, F., Chen, J., Huang, W., Chen, S., Huang, X., Jin, L., Jia, J., Zhang, X., An, C., Zhang, J., Zhao, Y., Yu, Z., Zhang, R., Liu, J., Zhou, A., Feng, S., 2019. Westerlies Asia and monsoonal Asia: spatiotemporal differences in climate change and possible mechanisms on decadal to sub-orbital timescales. Earth Sci. Rev. 192, 337–354.

Chen, J., Huang, W., Zhang, Q., Feng, S., 2020. Origin of the spatial consistency of summer precipitation variability between the Mongolian Plateau and the mid-latitude East Asian summer monsoon region. Sci. China Earth Sci. 63, 1199–1208.

Chiang, J.C.H., Kong, W., Wu, C.H., Battisti, D.S., 2020. Origins of East Asian summer monsoon seasonality. J. Clim. 33, 7945–7965.

Christenhusz, M.J.M., Reveal, J.L., Farjon, A., Gardner, M.F., Mill, R.R., Chase, M.W., 2011. A new classification and linear sequence of extant gymnosperms. Phytotaxa 19, 55–70.

Clift, P.D., Webb, A.A.G., 2018. A history of the Asian monsoon and its interactions with solid Earth tectonics in Cenozoic South Asia. In: Treloar, P.J., Searle, M.P. (Eds.), Himalayan Tectonics: A Modern Synthesis. London: Geological Society, Special Publications483, pp. 631–652.

Clift, P.D., Hodges, K.V., Heslop, D., Hannigan, R., Van Long, H., Calves, G., 2008. Correlation of Himalayan exhumation rates and Asian monsoon intensity. Nat. Geosci. 1, 875–880.

Cui, Y., Schubert, B.A., Jahren, A.H., 2020. A 23 m.y. record of low atmospheric CO_2. Geology 48, 888–892.

Ding, Y.-H., Chan, J.C.L., 2005. The East Asian summer monsoon: an overview. Meteorol. Atmos. Phys. 89, 117–142.

Ding, L., Spicer, R.A., Yang, J., Xu, Q., Cai, F., Li, S., Lai, Q., Wang, H., Spicer, T.E.V., Yue, Y., Shukla, A., Srivastava, G., Khan, M.A., Bera, S., Mehrotra, R., 2017. Quantifying the rise of the Himalaya orogen and implications for the South Asian monsoon. Geology 45, 215–218.

Doria, G., Royer, D.L., Wolfe, A.P., Fox, A., Westgate, J.A., Beerling, D.J., 2011. Declining atmospheric CO_2 during the late Middle Eocene climate transition. Am. J. Sci. 311, 63–75.

Ekart, D.D., 1999. A 400 million year carbon isotope record of pedogenic carbonate; implications for paleoatomospheric carbon dioxide. Am. J. Sci. 299, 805–827.

Fan, Y.-K., Wang, L., Su, T., Lan, Q.-Y., 2020. Spring drought as a possible cause for disappearance of native *Metasequoia* in Yunnan Province, China: Evidence from seed germination and seedling growth. Global Ecol. Conserv. 22 Article number: e00912.

Farnsworth, A., Lunt, D.J., Robinson, S.A., P.J.V, Roberts, W.H.G., Clift, P.D., Markwick, P., Su, T., Wrobel, N., Bragg, F., Kelland, S.-J., Pancost, R.D., 2019. Past East Asian monsoon evolution controlled by paleogeography, not CO_2. Sci. Adv. 5 Article number: eaax1697.

Farquhar, G.D., Sharkey, T.D., 1982. Stomatal conductance and photosynthesis. Annu. Rev. Plant Physiol. 33, 317–345.

Farquhar, G.D., Ehleringer, J.R., Hubick, K.T., 1989. Carbon isotope discrimination and photosynthesis. Annu. Rev. Plant Physiol. Plant Mol. Biol. 40, 503–537.

Foster, G.L., Lear, C.H., Rae, J.W.B., 2012. The evolution of pCO_2, ice volume and climate during the middle Miocene. Earth Planet. Sci. Lett. 341-344, 243–254.

Foster, G.L., Royer, D.L., Lunt, D.J., 2017. Future climate forcing potentially without precedent in the last 420 million years. Nat. Commun. 8 Article number: 14845.

Franks, P.J., Royer, D.L., Beerling, D.J., Van de Water, P.K., Cantrill, D.J., Barbour, M.M., Berry, J.A., 2014. New constraints on atmospheric CO_2 concentration for the Phanerozoic. Geophys. Res. Lett. 41, 4685–4694.

Fu, L.-G., Yu, Y.-F., Mill, R.R., 1999. Taxodiaceae. In: Wu, Z.-Y., Raven, P.H. (Eds.), Flora of China. Vol. 4 (Cycadaceae through Fagaceae). Science Press, Beijing and Missouri Botanical Garden Press, St. Louis, pp. 54–61.

Gébelin, A., Mulch, A., Teyssier, C., Jessup, M.J., Law, R.D., Brunel, M., 2013. The Miocene elevation of Mount Everest. Geology 41, 799–802.

Goldner, A., Herold, N., Huber, M., 2014. The challenge of simulating the warmth of the mid-Miocene climatic optimum in CESM1. Clim. Past 10, 523–536.

Greenop, R., Sosdian, S.M., Henehan, M.J., Wilson, P.A., Lear, C.H., Foster, G.L., 2019. Orbital forcing, ice-volume and CO_2 across the Oligocene-Miocene Transition. Paleoceanogr. Paleoclimatol. 34, 316–328.

Guo, Z.T., Ruddiman, W.F., Hao, Q.Z., Wu, H.B., Qiao, Y.S., Zhu, R.X., Peng, S.Z., Wei, J.J., Yuan, B.Y., Liu, T.S., 2002. Onset of Asian desertification by 22 Myr ago inferred from loess deposits in China. Nature 416, 159–163.

Guo, Z.T., Sun, B., Zhang, Z.S., Peng, S.Z., Xiao, G.Q., Ge, J.Y., Hao, Q.Z., Qiao, Y.S., Liang, M.Y., Liu, J.F., Yin, Q.Z., Wei, J.J., 2008. A major reorganization of Asian climate by the early Miocene. Clim. Past 4, 153–174.

Gupta, N.S., Yang, H., Leng, Q., Briggs, D.E.G., Cody, G.D., Summons, R.E., 2009. Diagenesis of plant biopolymers: decay and macromolecular preservation of *Metasequoia*. Org. Geochem. 40, 802–809.

Hansen, J., Sato, M., Russell, G., Kharecha, P., 2013. Climate sensitivity, sea level and atmospheric carbon dioxide. Phil. Trans. R. Soc. A 371 Article number: 20120294.

He, W., Xiao, L., Li, X., Guo, S., 2018. An ancient example of *Platycladus* (Cupressceae) from the early Miocene of northern China: origin and biogeographical implications. Hist. Biol. 30, 1123–1131.

Herold, N., Huber, M., Müller, R.D., Seton, M., 2012. Modeling the Miocene climatic optimum: Ocean circulation. Paleoceanography 27 Article number: PA1209.

IPCC, 2021. In: Masson-Delmotte, V., Zhai, P., Pirani, A., Connors, S.L., Péan, C., Berger, S., Caud, N., Chen, Y., Goldfarb, L., Gomis, M.I., Huang, M., Leitzell, K., Lonnoy, E., Matthews, J.B.R., Maycock, T.K., Waterfield, T., Yelekçi, O., Yu, R., Zhou, B. (Eds.), Climate Change 2021: The Physical Science Basis. Contribution of Working Group I to the Sixth Assessment Report of the Intergovernmental Panel on Climate Change. Cambridge University Press In Press.

Ji, S., Nie, J., Lechler, A., Huntington, K.W., Heitmann, E.O., Breecker, D.O., 2018. A symmetrical CO_2 peak and asymmetrical climate change during the middle Miocene. Earth Planet. Sci. Lett. 499, 134–144.

Johnstonea, J.A., Dawson, T.E., 2010. Climatic context and ecological implications of summer fog decline in the coast redwood region. Proc. Natl. Acad. Sci. 107, 4533–4538.

Jolivet, M., Ritz, J.-F., Vassallo, R., Larroque, C., Braucher, R., Todbileg, M., Chauvet, A., Sue, C., Arnaud, N., De Vicente, R., Arzhanikova, A., Arzhanikov, S., 2007. Mongolian summits: an uplifted, flat, old but still preserved erosion surface. Geology 35, 871–874.

Kerp, H., 1990. The study of fossil gymnosperms by means of cuticular analysis. Palaios 5, 548–569.

Konrad, W., Roth-Nebelsick, A., Grein, M., 2008. Modelling of stomatal density response to atmospheric CO_2. J. Theoret. Biol. 253, 638–658.

Konrad, W., Katul, G., Roth-Nebelsick, A., Grein, M., 2017. A reduced order model to analytically infer atmospheric CO_2 concentration from stomatal and climate data. Adv. Water Resour. 104, 145–157.

Konrad, W., Royer, D.L., Franks, P.J., Roth-Nebelsick, A., 2020. Quantitative critique of leaf-based paleo-CO_2 proxies: consequences for their reliability and applicability. Geol. J. 1–17.

Kowalczyk, J.B., Royer, D.L., Miller, I.M., Anderson, C.W., Beerling, D.J., Franks, P.J., Grein, M., Konrad, W., Roth-Nebelsick, A., Bowring, S.A., Johnson, K.R., Ramezani, J., 2018. Multiple proxy estimates of atmospheric CO_2 from an early Paleocene rainforest. Paleoceanogr. Paleoclimatol. 33, 1427–1438.

Kürschner, W.M., Kvaček, Z., Dilcher, D.L., 2008. The impact of Miocene atmospheric carbon dioxide fluctuations on climate and the evolution of terrestrial ecosystems. Proc. Natl. Acad. Sci. 105, 449–453.

Leng, Q., 2005. Cuticular analysis of living and fossil *Metasequoia*. In: LePage, B.A., Williams, C.J., Yang, H. (Eds.), The Geobiology and Ecology of *Metasequoia*. Springer Netherlands, Dordrecht and Norwell, pp. 197–217.

Leng, Q., Yang, H., Yang, Q., Zhou, J.-P., 2001. Variation of cuticle micromorphology of *Metasequoia glyptostroboides* (Taxodiaceae). Bot. J. Linn. Soc. 136, 207–219.

Leng, Q., Fan, S.-H., Wang, L., Yang, H., Lai, X.-L., Cheng, D.-D., Ge, J.-W., Shi, G.-L., Jiang, Q., Liu, X.-Q., 2007. Updated database of all known native *Metasequoia glyptostroboides* in South-Central China based on new census surveys and expeditions. Bull. Peabody Mus. Nat. Hist. Yale Univ. 48, 185–233.

LePage, B.A., Yang, H., Matsumoto, M., 2005. The evolution and biogeographic history of *Metasequoia*. In: LePage, B.A., Williams, C.J., Yang, H. (Eds.), The Geobiology and Ecology of *Metasequoia*. Springer Netherlands, Dordrecht and Norwell, pp. 3–114.

Levy, R., Harwood, D., Fabio, F., Sangiorgi, F., Tripati, R., Eynatten, H., Gasson, E., Kuhn, G., Tripati, A., DeConto, R., Fielding, C., Field, B., Golledge, N., McKay, R., Naish, T., Olney, M., Pollard, D., Schouten, S., Talarico, F., Cornamusini, G., 2016. Antarctic ice sheet sensitivity to atmospheric CO_2 variations in the early to mid-Miocene. Proc. Natl. Acad. Sci. 113, 3453–3458.

Li, C.-K., 1962. A Tertiary beaver from Changpei, Hopei Province. Vertebr. Palasiat. 6, 72–77 (in Chinese with English summary).

Li, D.-M., Li, Q., 2003. Serial K-Ar dating along the volcanic section in Zuoyun, Shanxi Province. Acta Geoscient. Sin. 24, 559–562 (in Chinese with English abstract).

Li, H.M., Yang, G.Y., 1984. A Miocene flora from Qiuligou, Jilin. Acta Palaeontol. Sin. 23, 204–213 (in Chinese with English abstract).

Li, H., Yu, J.-X., McElwain, J.C., Yiotis, C., Chen, Z.-Q., 2019. Reconstruction of atmospheric CO_2 concentration during the late Changhsingian based on fossil conifers from the Dalong Formation in South China. Palaeogeogr. Palaeoclimatol. Palaeoecol. 519, 37–48.

Liang, J.-Q., Leng, Q., Höfig, D.F., Niu, G., Wang, L., Royer, D.L., Burke, K., Xiao, L., Zhang, Y.-G., Yang, H., 2022. Constraining conifer physiological parameters in leaf gas-exchange models for ancient CO_2 reconstruction. Global Planet. Change 209 Article number: 103737.

Licht, A., van Cappelle, M., Abels, H.A., Ladant, J.B., Trabucho-Alexandre, J., France-Lanord, C., Donnadieu, Y., Vandenberghe, J., Rigaudier, T., Lecuyer Jr., C., D.T, Adriaens, R., Bourn, A., Guo, Z., Soe, A.N., Quade, J., Dupont-Nivet, G., Jaeger, J.-J., 2014. Asian monsoons in a late Eocene greenhouse world. Nature 513, 501–506.

Liu, Y.-S., Basinger, J.F., 2009. *Metasequoia* HU et CHENG (Cupressaceae) from the Eocene of Axel Heiberg Island, Canadian High Arctic. Palaeontogr. Abt. B Palaeobot. 282, 69–97.

Liu, X., Yin, Z.Y., 2002. Sensitivity of East Asian monsoon climate to the uplift of the Tibetan Plateau. Palaeogeogr. Palaeoclimatol. Palaeoecol. 183, 223–245.

Liu, Y.-S., Utescher, T., Zhou, Z.-K., Sun, B.-N., 2011. The evolution of Miocene climates in North China: preliminary results of quantitative reconstructions from plant fossil records. Palaeogeogr. Palaeoclimatol. Palaeoecol. 304, 308–317.

Londoño, L., Royer, D.L., Jaramillo, C., Escobar, J., Foster, D.A., Cárdenas-Rozo, A.L., Wood, A., 2018. Early Miocene CO_2 estimates from a Neotropical fossil leaf assemblage exceed 400 ppm. Am. J. Bot. 105, 1–9.

Lowenstein, T.K., Demicco, R.V., 2006. Elevated Eocene atmospheric CO_2 and its subsequent decline. Science 313, 1928.

Ma, Q.-W., Li, C.-S., 2002a. Characteristics of reference in classifying fossil plants of genera *Metasequoia* and *Sequoia* by epidermal features. J. Wuhan Bot. Res. 20, 413–416.

Ma, Q.-W., Li, C.-S., 2002b. Epidermal structures of *Sequoia sempervirens* (D. Don) Endl. (Taxodiceae). Taiwania 47, 194–202.

Ma, Q.-W., Li, F.-L., Li, C.-S., 2005. The coast redwoods (*Sequoia*, Taxodiaceae) from the Eocene of Heilongjiang and the Miocene of Yunnan, China. Rev. Palaeobot. Palynol. 135, 117–129.

Ma, Q.-W., Ferguson, D.K., Liu, H.M., Xu, J.X., 2021. Compressions of *Sequoia* (Cupressaceae *sensu lato*) from the Middle Jurassic of Daohugou, Ningcheng, Inner Mongolia, China. Palaeobiodiv. Palaeoenviron. 101, 25–33.

Maxbauer, D.P., Royer, D.L., LePage, B.A., 2014. High Arctic forests during the middle Eocene supported by moderate levels of atmospheric CO_2. Geology 42, 1027–1030.

Miao, J.-P., Wang, T., Chen, D., 2020. More robust changes in the East Asian winter monsoon from 1.5 to 2.0°C global warming targets. Int. J. Climatol. 40, 1–19.

Milligan, J.N., Royer, D.L., Franks, P.J., Upchurch, G.R., McKee, M.L., 2019. No evidence for a large atmospheric CO_2 spike across the Cretaceous-Paleogene boundary. Geophys. Res. Lett. 46, 3462–3472.

Noss, R.F., 2000. The Redwood Forest: History, Ecology, and Conservation of the Coast Redwoods (Save-the-Redwoods League). Island Press, Washington, D. C.

O'Brien, C.L., Huber, M., Thomas, E., Pagani, M., Super, J.R., Elder, L.E., Hull, P.M., 2020. The enigma of Oligocene climate and global surface temperature evolution. Proc. Natl. Acad. Sci. 117, 25302–25309.

Olson, D.F., Roy, D.F., Walters, G.A., 1990. *Sequoia sempervirens* (D.Don) Endl. Redwood. In: Burns, R.M., Honkala, B.H. (Eds.), Silvices of North America. USDA Forest Service, Washington DC, pp. 541–551.

Pagani, M., Huber, M., Liu, Z., Bohaty, S.M., Henderiks, J., Sijp, W., Krishnan, S., DeConto, R.M., 2011. The role of carbon dioxide during the onset of Antarctic glaciation. Science 334, 1261–1264.

Palcu, D.V., Patina, I.S., Şandric, I., Lazarev, S., Vasiliev, I., Stoica, M., Krijgsman, W., 2021. Late Miocene megalake regressions in Eurasia. Scient. Rep. 11 Article number: 11471.

Piao, J., Chen, W., Zhang, Q., Hu, P., 2018. Comparison of moisture transport between Siberia and Northeast Asia on annual and interannual time scales. J. Clim. 31, 7645–7660.

Rae, J.W.B., Zhang, Y.G., Liu, X., Foster, G.L., Whiteford, R.D.M., 2021. Atmospheric CO_2 over the past 66 million years from marine archives. Annu. Rev. Earth Planet. Sci. 49, 609–641.

Ralph, J., Hatfield, R.D., 1991. Pyrolysis-GC-MS characterization of forage materials. J. Agric. Food Chem. 39, 1426–1437.

Raymo, M.E., Ruddiman, W.F., 1992. Tectonic forcing of late Cenozoic climate. Nature 359, 117–122.

Reichgelt, T., D'Andrea, W.J., 2019. Plant carbon assimilation rates in atmospheric CO_2 reconstructions. New Phytol. 223, 1844–1855.

Reichgelt, T., D'Andrea, W.J., Fox, B.R.S., 2016. Abrupt plant physiological changes in southern New Zealand at the termination of the Mi-1 event reflect shifts in hydroclimate and pCO_2. Earth Planet. Sci. Lett. 455, 115–124.

Reichgelt, T., D'Andrea, W.J., Valdivia-McCarthy, A.d.c., Fox, B.R.S., Bannister, J.M., Conran, J.G., Lee, W.G., Lee, D.E., 2020. Elevated CO_2, increased leaf-level productivity, and water-use efficiency during the early Miocene. Clim. Past 16, 1509–1521.

Royer, D.L., Wing, S.L., Beerling, D.J., Jolley, D.W., Koch, P.L., Hickey, L.J., Berner, R.A., 2001. Paleobotanical evidence for near present-day levels of atmospheric CO_2 during part of the Tertiary. Science 292, 2310–2313.

Royer, D.L., Moynihan, K.M., McKee, M.L., Londoño, L., Franks, P.J., 2019. Sensitivity of a leaf gas-exchange model for estimating paleoatmospheric CO_2 concentration. Clim. Past 15, 795–809.

Salisbury, E.J., 1928. On the causes and ecological significance of stomatal frequency, with special reference to the woodland flora. Philos. Trans. R. Soc. Lond. B. 216, 1–65.

Sampe, T., Xie, S.-P., 2010. Large-scale dynamics of the Meiyu-Baiu Rainband: Environmental forcing by the westerly jet. J. Clim. 23, 113–134.

Schellnhuber, H.J., Rahmstorf, S., Winkelmann, R., 2016. Why the right climate target was agreed in Paris. Nat. Clim. Change 6, 649–653.

Sha, Y.-Y., Shi, Z.-G., Liu, X.-D., An, Z.-S., 2015. Distinct impacts of the Mongolian and Tibetan Plateaus on the evolution of the East Asian monsoon. J. Geophys. Res. Atmos. 120, 4764–4782.

Shi, Z.-G., Liu, X.-D., Liu, Y.-M., Sha, Y.-Y., Xu, T.-T., 2015. Impact of Mongolian Plateau versus Tibetan Plateau on the westerly jet over North Pacific Ocean. Clim. Dyn. 44, 3067–3076.

Sigovini, M., Keppel, E., Tagliapietra, D., 2016. Open nomenclature in the biodiversity era. Meth. Ecol. Evol. 7, 1217–1225.

Sosdian, S.M., Greenop, R., Hain, M.P., Foster, G.L., Pearson, P.N., Lear, C.H., 2018. Constraining the evolution of Neogene ocean carbonate chemistry using the boron isotope pH proxy. Earth Planet. Sci. Lett. 498, 362–376.

Spicer, R.A., Yang, J., Herman, A.B., Kodrul, T., Maslova, N., Spicer, T., Aleksandrova, G., Jin, J., 2016. Asian Eocene monsoons as revealed by leaf architectural signatures. Earth Planet. Sci. Lett. 449, 61–68.

Spicer, R.A., Su, T., Valdes, P.J., Farnsworth, A., Wu, F.-X., Shi, G., Spicer, T.E.V., Zhou, Z., 2021. Why 'the uplift of the Tibetan Plateau' is a myth. Natl. Sci. Rev. 8 Article number: nwaa091.

Steininger, F.F., Rögl, F., 1984. Paleogeography and palinspastic reconstruction of the Neogene of the Mediterranean and Paratethys. Geol. Soc. Lond. Spec. Publ. 17, 659–668.

Steinthorsdottir, M., Vajda, V., Pole, M., 2019. Significant transient pCO_2 perturbation at the New Zealand Oligocene-Miocene transition recorded by fossil plant stomata. Palaeogeogr. Palaeoclimatol. Palaeoecol. 515, 152–161.

Steinthorsdottir, M., Coxall, H., De Boer, A., Huber, M., Barbolini, N., Bradshaw, C., Burls, N., Feakins, S., Gasson, E., Henderiks, J., Holbourn, A.E., Kiel, S., Kohn, M., Knorr, G., Kürschner, W., Lear, C., Liebrand, D., Lunt, D.J., Mörs, T., Pearson, P., Pound, M.J., Heather, S., Stromberg, C., 2021a. The Miocene: the future of the past. Paleoceanogr. Paleoclimatol. 36 Article number: e2020PA004037.

Steinthorsdottir, M., Jardine, P.E., Rember, W.C., 2021b. Near-future *p*CO2 during the hot Mid Miocene Climatic Optimum. Paleoceanogr. Paleoclimatol. 36 Article number: e2020PA003900.

Sun, H., Liu, X.-D., 2018. Impacts of the uplift of four mountain ranges on the arid climate and dust cycle of inland Asia. Palaeogeogr. Palaeoclimatol. Palaeoecol. 505, 167–179.

Sun, X.-J., Wang, P.-X., 2005. How old is the Asian monsoon system? - Palaeobotanical records from China. Palaeogeogr. Palaeoclimatol. Paleoecol. 222, 181–222.

Sun, J.M., Li, Y., Zhang, Z.Q., Fu, B.H., 2009. Magnetostratigraphic data on Neogene growth folding in the foreland basin of the southern Tianshan Mountains. Geology 37, 1051–1054.

Super, J.R., Thomas, E., Pagani, M., Huber, M., O'Brien, C., Hull, P.M., 2018. North Atlantic temperature and pCO_2 coupling in the early-middle Miocene. Geology 46, 519–522.

Tada, R., Zheng, H.-B., Clift, P.D., 2016. Evolution and variability of the Asian monsoon and its potential linkage with uplift of the Himalaya and Tibetan Plateau. Prog. Earth Planet. Sci. 3 Article number: 4.

Tan, X., Dilcher, D.L., Wang, H., Zhang, Y., Na, Y.L., Li, T., Li, Y.F., Sun, C.L., 2018. *Yanliaoa*, an extinct genus of Cupressaceae *s.l.* from the Middle Jurassic, northeastern China. Palaeoworld 27, 360–373.

Tang, H., Micheels, A., Eronen, J.T., Ahrens, B., Fortelius, M., 2013. Asynchronous responses of East Asian and Indian summer monsoons to mountain uplift shown by regional climate modelling experiments. Clim. Dynam. 40, 1531–1549.

Tesfamichael, T., Jacobs, B., Tabor, N., Michel, L., Currano, E., Feseha, M., Barclay, R., Kappelman, J., Schmitz, M., 2017. Settling the issue of "decoupling" between atmospheric carbon dioxide and global temperature: $[CO_2]_{atm}$ reconstructions across the warming Paleogene-Neogene divide. Geology 45, 999–1002.

Thomson, J.R., Holden, P.B., Anand, P., Edwards, N.R., Porchier, C.A., Harris, N.B.W., 2021. Tectonic and climatic drivers of Asian monsoon evolution. Nat. Commun. 12 Article number: 4022.

Thumma, J.K., 2016. Assessing the timing of intracontinental uplift of the Gobi Altai, Mongolia using low-temperature thermochronology. M.S. ThesisLehigh University.

Vassallo, R., Jolivet, M., Ritz, J.-F., Braucher, R., Larroque, C., Sue, C., Todbileg, M., Javkhlanbold, D., 2007. Uplift age and rates of the Gurvan Bogd system (Gobi-Altay) by apatite fission track analysis. Earth Planet. Sci. Lett. 259, 333–346.

Wang, L., 2010. Morphology and anatomy of *Metasequoia* leaves and their environmental indicative values: Evidence from the comparative studies of "living fossil" and fossils. Ph.D. ThesisNanjing Institute of Geology and Palaeontology Nanjing and The Graduate University of Chinese Academy of Sciences (in Chinese with English summary).

Wang, L., Leng, Q., 2011. A new method to prepare clean cuticular membrane from fossil leaves with thin and fragile cuticles. Sci. China Earth Sci. 54, 223–227.

Wang, H.-F., Dai, T.-M., Fan, S.-K., Yang, X.-C., 1985. K-Ar dating of Hannuoba Basalts at Zhangjiakou. Geochimica 3, 206–215 (in Chinese with English abstract).

Wang, C., Dai, J., Zhao, X., Li, Y., Graham, S.A., He, D., Ran, B., Meng, J., 2014. Outward-growth of the Tibetan Plateau during the Cenozoic: a review. Tectonophysics 621, 1–43.

Wang, Y.-Q., Momohara, A., Wang, L., Lebreton-Anberrée, J., Zhou, Z.-K., 2015. Evolutionary history of atmospheric CO_2 during the Late Cenozoic from fossilized *Metasequoia* needles. PLoS One 10 Article number: e0130941.

Wang, L., Kunzmann, L., Su, T., Xing, Y.-W., Zhang, S.-T., Wang, Y.-Q., Zhou, Z.-K., 2019. The disappearance of *Metasequoia* (Cupressaceae) after the middle Miocene in Yunnan, Southwest China: evidences for evolutionary stasis and intensification of the Asian monsoon. Rev. Palaeobot. Palynol. 264, 64–74.

Wang, Y.-Q., Wang, L., Momohara, A., Leng, Q., Huang, Y.-J., 2020. The Paleogene atmospheric CO_2 concentrations reconstructed using stomatal analysis of fossil *Metasequoia* needles. Palaeoworld 29, 744–751.

Westerhold, T., Marwan, N., Drury, A.J., Liebrand, D., Agnini, C., Anagnostou, E., Barnet, J.S.K., Bohaty, S.M., Vleeschouwer, D.D., Florindo, F., Frederichs, T., Hodell, D.A., Holbourn, A.E., Kroon, D., Lauretano, V., Littler, K., Lourens, L.J., Lyle, M., Pälike, H., Röhl, U., Tian, J., Wilkens, R.H., Wilson, P.A., Zachos, J.C., 2020. An astronomically dated record of Earth's climate and its predictability over the last 66 million years. Science 369, 1383–1387.

White, R.H., Battisti, D.S., Sheshadri, A., 2018. Orography and the boreal winter stratosphere: The importance of the Mongolian mountains. Geophys. Res. Lett. 45, 2088–2096.

Witkowski, C.R., Gupta, N.S., Yang, H., Leng, Q., Williams, C.J., Briggs, D.E.G., Summons, R.E., 2012. Molecular preservation of cenozoic conifer fossil *Lagerstätten* from banks island, the Canadian arctic. Palaios 27, 279–287.

Witkowski, C.R., Weijers, J., Blais, B., Schouten, S., Sinninghe Damsté, J.S., 2018. Molecular fossils from phytoplankton reveal secular pCO_2 trend over the Phanerozoic. Sci. Adv. 4 Article number: eaat4556.

Witkowski, C.R., Leng, Q., Reid, C.W., Feng, L., Yang, H., 2022. Tissue decay tested in modern *Metasequoia* leaves: implications for early diagenesis of leaves in fossil *Lagerstätten*. Rev. Palaeobot. Palynol. 304 Article number: 104720..

Yang, H., Hickey, L.J., 2007. *Metasequoia*: back from the brink? An update-proceedings of the second international symposium on *Metasequoia* and associated plants. New Haven Bull. Peobody Mus. Nat. Hist. Yale Univ. 48 (2), 183–426.

Yang, H., Jin, J.-H., 2000. Phytogeographic history and evolutionary stasis of *Metasequoia*: geological and genetic information contrasted. Acta Palaeontol. Sin. 39 (Supplements), 288–307.

Yang, H., Huang, Y.-S., Leng, Q., LePage, B.A., Williams, C.J., 2005. Biomolecular preservation of Tertiary *Metasequoia* fossil *Lagerstätten* revealed by comparative pyrolysis analysis. Rev. Palaeobot. Palynol. 134, 237–256.

Yang, H., Leng, Q., LePage, B.A., 2007. Labile biomolecules in three-dimensionally preserved early Tertiary *Metasequoia* leaves from Ellesmere Island, Canada. Bulle. Peabody Mus. Nat. Hist. Yale Univ. 48, 317–327.

Yang, H., Pagani, M., Briggs, D.E.G., Equiza, M.A., Jagels, R., Leng, Q., LePage, B.A., 2009. Carbon and hydrogen isotope fractionations under continuous light: implications for paleoenvironmental interpretations of the High Arctic during Paleogene warming. Oecologia 160, 461–470.

Yang, B., Qin, C., Bräuning, A., Osborn, T.J., Trouet, V., Ljungqvist, F.C., Esper, J., Schneider, L., Grießinger, J., Büntgenl, U., Rossi, S., Dong, G., Yan, M., Ning, L., Wang, J., Wang, X., Wang, S., Luterbacher, J., Cook, E.R., Stenseth, N.C., 2021. Long-term decrease in Asian monsoon rainfall and abrupt climate change events over the past 6,700 years. Proc. Natl. Acad. Sci. 118 Article number: e2102007118.

Yu, E.-T., Zhang, R., Jiang, D.-B., Ramstein, G., Zhang, Z.-S., Sun, J.-Q., 2018. High-resolution simulation of Asian monsoon response to regional uplift of the Tibetan Plateau with regional climate model nested with global climate model. Global Planet. Change 169, 34–47.

Zhang, W., Han, B., 2006. K–Ar chronology and geochemistry of Jining Cenozoic basalts, Inner Mongolia, and geodynamic implications. Acta Petyol. Sin. 22, 1597–1607 (In Chinese with English abstract).

Zhang, Z., Sun, J., 2011. Palynological evidence for Neogene environmental change in the foreland basin of the southern Tianshan range, northwestern China. Global Planetary Change 75, 55–56.

Zhang, Y.G., Pagani, M., Liu, Z., Bohaty, S.M., Deconto, R., 2013. A 40-million-year history of atmospheric CO_2. Phil. Trans. R. Soc. A 371 Article number: 20130096.

Zhang, J.-W., D'rozario, A., Adams, J.M., Li, Y., Liang, X.-Q., Jacques, F.M., Su, T., Zhou, Z.-K., 2015. *Sequoia maguanensis*, a new Miocene relative of the coast redwood, *Sequoia sempervirens*, from China: implications for paleogeography and paleoclimate. Am. J. Bot. 102, 103–118.

Zhang, R., Jiang, D.-B., Zhang, Z.-S., Cheng, Z.-G., Zhang, Q., 2017. Comparison of the climate effects of surface uplifts from the northern Tibetan Plateau, the Tianshan, and the Mongolian Plateau on the East Asian climate. J. Geophys. Res. Atmos. 122, 7949–7970.

Zhao, Z.-X., Wang, Y., Zang, Z.-H., Deng, S.-Y., Lan, T.-Y., Xie, Z.-Q., Xiong, G.-M., Li, J.-Q., Shen, G.-Z., 2020. Climate warming has changed phenology and compressed the climatically suitable habitat of *Metasequoia glyptostroboides* over the last half century. Global Ecol. Conserv. 23 Article number: e01140.

Zhou, N., Wang, Y.-D., Ya, L., Porter, A.S., Kürschner, W.M., Li, L.-Q., Lu, N., McElwain, J.C., 2020. An inter-comparison study of three stomatal-proxy methods for CO_2 reconstruction applied to early Jurassic Ginkgoales plants. Palaeogeogr. Palaeoclimatol. Palaeoecol. 542, 109547.